Mineralium Deposita
https://doi.org/10.1007/s00126-025-01353-z

ARTICLE

Orogenic arc-related Ni-Cu-(PGE) mineralization of the Ransko massif, Czech Republic, and implications for the metallogeny of the European Variscan belt

Lukáš Ackerman[1,2] · Vojtěch Wertich[1,3] · Jan Pašava[1] · Martin Kubeš[1,3] · Petr Rambousek[1] · Jitka Míková[1] · Jiří Sláma[2] · Václav Santolík[2] · Andreas Pack[4] · Robert A. Creaser[5] · Karel Malý[6] · Tomáš Magna[1]

Received: 18 October 2024 / Accepted: 16 February 2025

Abstract

The Ransko (ultra)mafic massif, Bohemian Massif, Czech Republic, hosts several Ni–Cu–(PGE) deposits and peculiar Zn–Cu–Ba ores. Geochronology integrated with petrography, bulk-rock, and mineral compositions together with Sr–Nd–Pb–Hf–Os–O isotopic systematics of barren and variably mineralized (ultra)mafic lithologies as well as massive ores reveal a complex evolution of the Ransko massif and its mineralizations. The Sm–Nd and U–Pb ages obtained for gabbros and cross-cutting granite porphyry, respectively, overlap with Re–Os ages of Ni–Cu–(PGE) and Zn–Cu ores and limit the formation age of (ultra)mafic rocks and metal accumulations to ~ 370–345 Ma. Compositional variations indicate derivation of parental melts of the Ransko massif from metasomatized, Variscan sub-arc mantle and underscore the importance of assimilation–fractional crystallization and crystal accumulation processes. The Ni–Cu ores were emplaced through the gravity-driven percolation of dense sulfide liquids along previously weakened structures associated with the downward crystal fractionation. The orogenic and arc-related nature of the Ransko Ni–Cu–(PGE) mineralization shares some remarkable similarities with some other Ni–Cu deposits in the European Variscan Belt highlighting the significance of these deposits emplaced in arc-related crustal domains. Yet, the variable nature of these mineralizations indicates complex processes that happen during the emplacement and evolution of the parental magmas driving their favourable metal contents.

Keywords Orogenic · Gabbro · Zn–Cu · Ni–Cu–PGE · Metallogeny · Variscan

Introduction

Magmatic sulfide deposits represent one of the most important sources of Ni and Cu as well as platinum-group elements (PGE) and Co (e.g., Keays and Lightfoot 2010; Naldrett 2010; Li and Ripley 2011a; Lu et al. 2019; Gao and Wang 2024). Most economic occurrences are related to Archean–Proterozoic intra-plate (ultra)mafic magmatism forming world-class deposits (Naldrett 2010) that are associated either with komatiites, picrites, and flood basalts (e.g., Kambalda, Duluth, Noril'sk/Pechenga or Jinchuan) or gabbroic-granitic rocks (Voisey's Bay and Sudbury). On the other hand, arc-related, orogenic type Ni–Cu–(Co–PGE) deposits sometimes bound to Alaskan-type complexes have been rather overlooked because of their typically low economic significance (Naldrett 2010). Nevertheless, due to an increasing demand for Ni, PGE, Co, and Cu required for high-tech industry, several targeted studies have been pursued dealing with the exploration of arc-related

Editorial handling: B. Lehmann

✉ Lukáš Ackerman
ackerman@gli.cas.cz

1 Czech Geological Survey, Klárov 3, 118 21 Praha 1, Czech Republic

2 Institute of Geology of the Czech Academy of Sciences, Rozvojová 269, 165 00 Praha 6, Czech Republic

3 Department of Geological Sciences, Masaryk University, Kotlářská 2, 611 37, Brno, Czech Republic

4 Geowissenschaftliches Zentrum, Universität Göttingen, Goldschmidtstraße 1, D-37077, Göttingen, Germany

5 Department of Earth and Atmospheric Sciences, Faculty of Science, University of Alberta, Edmonton, Canada

6 Vysočina Museum Jihlava, Masarykovo náměstí 1224/55, 586 01 Jihlava, Czech Republic

Published online: 28 February 2025

Ni–Cu–(Co–PGE) deposits focusing on their ages, petrogenesis and significance for ore mineralization (e.g., Barnes et al. 2020; Jesus et al. 2020; Gao and Wang 2024; Zhao et al. 2024).

Arc-related orogenic Ni–Cu–(Co–PGE) deposits spanning the ages from > 2 Ga to the Phanerozoic have been identified in a number of places worldwide (e.g., Thakurta et al. 2008; Maier et al. 2008; Peltonen 1995; Gao and Wang 2024 and references therein). Gao and Wang (2024) noted that orogenic-type intrusions that host accumulations of Ni–Cu–(Co–PGE) ores share some characteristics such as the presence of orthopyroxene-rich lithologies or emplacement along fault systems in the form of elongated bodies. However, these characteristics do not apply to all arc-related intrusions as for example, some Alaskan-type complexes are predominantly formed by clinopyroxene, amphibole and/or olivine-rich lithologies (e.g., Johan 2002 and references therein). This hints at a rather diverse petrogenetic evolution of individual orogenic-type (ultra)mafic complexes in response to different sources, compositions, and evolution of parental melts, local tectonic settings, and/or pressure–temperature (P–T) conditions.

The Variscan orogenic massifs dispersed from Western to Central Europe are characterized by widespread arc-related magmatism (Janoušek et al. 2004; Ribeiro et al. 2007; Žák et al. 2014). Previous studies documented the presence of ~ 350–340 Ma (ultra)mafic bodies (Beja and Aguablanca) with sub-economic to economic Ni–Cu–(Co–PGE) mineralizations, respectively (Piña 2019; Jesus et al. 2020), that appear to be contemporaneous with large-scale arc-related granitic activity. In the Bohemian Massif, the exceptional case of the Variscan-related (ultra)mafic magmatic activity has been documented at the Ransko massif that hosts several Ni–Cu–(PGE) deposits as well as peculiar association with Zn–Cu–Ba ores (Mísař 1974; Pašava et al. 2003). However, modern studies conducted so far have been predominantly focused on PGE and Re–Os systematics (Pašava et al. 2003, 2023; Ackerman et al. 2013) with only limited information about the petrogenesis of the massif itself in terms of geotectonic settings, parental melt evolution and nature of sulfidic mineralizations.

In this study, we report combined U–Pb, Sm–Nd, and Re–Os geochronology coupled with major, trace and highly siderophile element compositions, paralleled by Sr–Nd–Pb–Hf–O isotopic determinations, of all known Ransko rock types to reveal the nature of magmatism and associated Ni–Cu–(PGE) ores as well as timing of Zn–Cu–Ba mineralizations. Using this integrated approach, our study explores the affinity of the Ransko mantle-derived parental magmas and the relationship of Ni–Cu–(PGE) and Zn–Cu–Ba mineralizations to widespread arc-related magmatic and hydrothermal activity, both closely related to the Variscan orogeny in the Bohemian Massif.

Geological background

The Bohemian Massif is traditionally divided into four tectonometamorphic units: the Saxothuringian, the Teplá–Barrandian, the Moldanubian, and Moravo-Silesian/Brunovistulian (e.g., Matte 2001; Schulmann et al. 2022; Fig. 1a). The Ransko massif is positioned in a transition zone between the Moldanubian Unit to the south, the Kutná Hora Crystalline Complex to the northwest, the Nasavrky Plutonic Complex to the north and the Hlinsko Zone to the east (Fig. 1b,c). The Kutná Hora Crystalline Complex shares some similarities in terms of lithology, P–T conditions (granulite, migmatite, peridotite-pyroxenite) and age with ~ 350–330 Ma high-grade metamorphic rocks of the Gföhl Unit of the Moldanubian Unit (Synek and Oliveriová 1993; Ackerman et al. 2020; Nahodilová et al. 2020). Similarly, the northerly located granitic rocks of the Nasavrky Plutonic Complex have similar calc-alkaline I-type composition and Re–Os age of disseminated molybdenite (Ackerman et al. 2017) to more westerly situated ~ 354–346 Ma Central Bohemian Plutonic Complex (CBPC; Žák et al. 2014). On the other hand, the adjacent, southern part of the Hlinsko Zone composed of (meta) volcanosedimentary rocks (phyllite) of the Vítanov Formation is assumed to be Neoproterozoic in age (Pitra and Guiraud 1996).

The Ransko massif with the assumed age of ~ 342 Ma (Re–Os; Ackerman et al. 2013) occupies the area of approximately 10 km^2 and consists of two main lithological units: (1) peridotite (dunite; Fig. 2a) accompanied by troctolite, olivine gabbro, and (2) olivine/amphibole-bearing gabbro (Fig. 1c) with rare anorthosite altogether sometimes penetrated by quartz diorite (Mísař 1974). In the eastern part of the massif, the swarm of granite and/or syenite porphyry dykes crosscutting the (ultra)mafic lithologies is present (Fig. 1c). According to Mísař (1974), the Ransko parental magmas underwent two-stage differentiation. First, magmas formed through partial melting of a slightly depleted mantle (Pašava et al. 2003) evolved at a deep magma chamber during an intense assimilation–fractional crystallization process associated with sulfide liquid immiscibility. Second, such magmas ascended to the shallower crustal levels and their emplacement was further associated with a second stage of assimilation–fractional crystallization.

Predominantly disseminated to locally semi-massive/massive Ni–Cu–(PGE) ore bodies were discovered during extensive drilling campaigns in the past at several locations in the Ransko massif (e.g., deposits Jezírka, Doubravka, Řeka, Tůně; Fig. 1c), forming a discontinuous, up to 3 km long and 1 km wide mineralized zone in a NE–SW direction (Mísař 1974). In general, all these ore

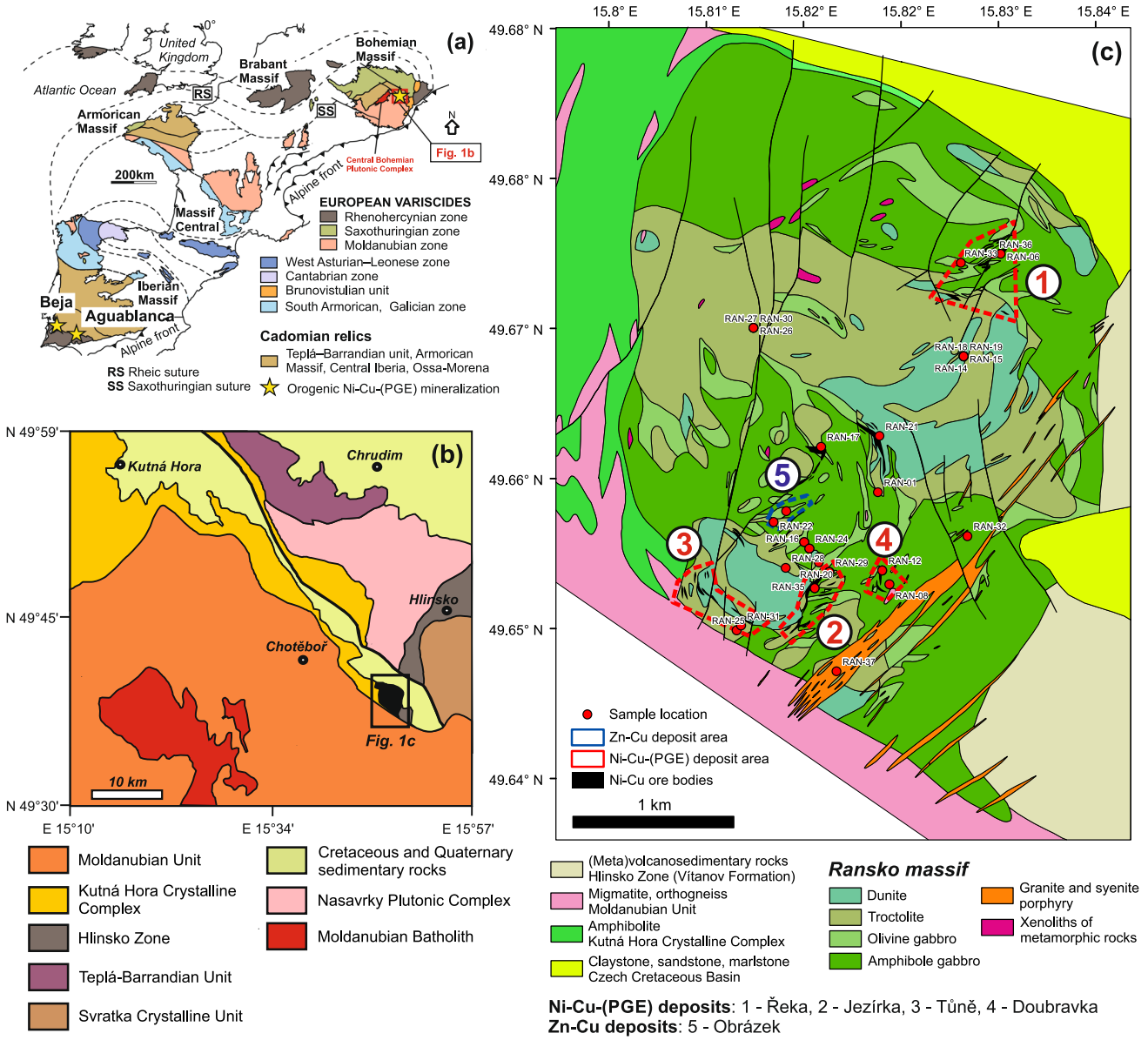

Fig. 1 (**a**) Simplified geological map showing the distribution of European Variscan Belt relicts dispersed from Western to Central Europe. (**b**) Geological settings of the Ransko massif within a broader context of surrounding formations (adopted and modified from Štědrá et al. 2009). (**c**) Geological map of the Ransko massif with locations of studied samples and Ni–Cu–(PGE) and Zn–Cu deposits marked

bodies are predominantly composed of pyrrhotite, pentlandite and chalcopyrite (Pašava et al. 2003) with total Ni and Cu contents reaching up to 4 wt% while elevated Pt and Pd contents (up to ~ 0.7 ppm) are related to the presence of michenerite, froodite, and sperrylite. The bodies are predominantly located in the largely altered contact zones between troctolite and gabbro. Furthermore, during prospection for Ni–Cu ores, the Zn–Cu deposit (Obrázek) associated with the intrusion of quartz diorite into the (ultra)mafic Ransko cumulate rocks was discovered during the drilling campaign (Mísař 1974).

Samples and methodology

In total, 32 samples representative of all (ultra)mafic lithologies including samples with either massive or disseminated Ni–Cu–(PGE) mineralizations, one sample of granite porphyry cross-cutting the massif (Fig. 1c), two samples of massive Zn–Cu ore (Obrázek deposit) and two leucocratic xenoliths representing country rocks were selected for this study. The majority of rock samples have been obtained from several drill cores at variable depths,

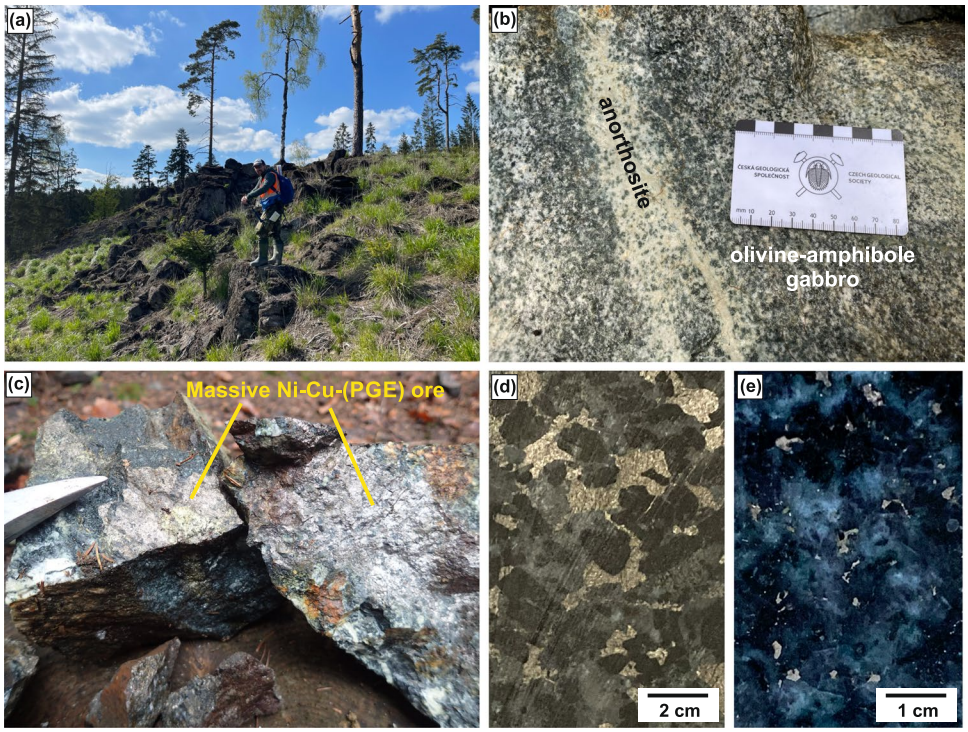

Fig. 2 Photographs illustrating some examples of (ultra)mafic rocks and related Ni–Cu–(PGE) ores of the Ransko massif. (**a**) An outcrop of strongly serpentinized dunite (locality Tůně, 49.65° N, 15.81° E). (**b**) A close-up view of the representative sample of olivine–amphibole gabbro with accumulation of plagioclase forming anorthosite (locality Hluboká, 49.66° N, 15.84° E). (**c**) representative examples of massive Ni–Cu–(PGE) ore (sample RAN-34) collected at the Jezírka deposit dump (Shaft No. 1, Jezírka deposit, 49.65° N, 15.82° E. (**d**, **e**) illustrative examples of semi-massive, net-texture (**d**) and disseminated (**e**) Ni–Cu–(PGE) ores (Jezírka and Řeka deposits, respectively)

deposited at the Czech Geological Survey (CGS) with additional samples either gathered from rock collections at the Faculty of Science, Charles University (anorthosite) or newly collected in the field (see Supplementary Table 1 for details).

Major and trace element compositions were determined using wet-chemistry (CGS) and ICP-MS (Faculty of Science, Charles University) techniques following the methods detailed in Dempírová et al. (2010) and Strnad et al. (2005), respectively. The overall precision of major element analyses was always better than ± 5% while the accuracy monitored through the periodical analyses of JG-3 reference material (USGS) yielded values better than 10% (RSD). The solution ICP-MS technique yielded precision and accuracy better than ± 1% and 10–15% (RSD), respectively, monitored through the analyses of BCR-2 reference material (USGS).

Major element compositions of mineral phases were determined using the Cameca SX 100 electron microprobe (EMP) at the Masaryk University with the operating conditions as follows: wavelength-dispersive mode, an accelerating voltage of 15 kV, a beam current of 10–20 nA, and a beam size of 2–5 µm (see Kubeš et al. 2022 for more details).

The Sm–Nd geochronology and Sr–Nd–Pb isotopic analyses were carried out at the Institute of Geology of the Czech Academy of Sciences (IG CAS). The Sr–Nd–Pb isotopic protocol detailed in Ackerman et al. (2020) involves the decomposition of samples followed by Sr, Nd, and Pb isolation by means of ion-exchange chromatography using the methodology of Pin et al. (2014) and subsequent isotopic analyses using a *Triton Plus* thermal ionization mass spectrometer (TIMS; Thermo). For Sm–Nd geochronology, mineral separates and corresponding whole-rocks were digested with ^{150}Nd–^{149}Sm spike. Thereafter, Sm and Nd were isolated by a combination of TRU and LN resins (Pin et al. 2014), and their isotopic compositions were analyzed using a *Triton Plus* TIMS with double Re and Ta–Re filament assembly, respectively. The Lu–Hf isotopic data were acquired following the methods summarized in Ackerman et al. (2020) involving sample decomposition followed by ion-exchange column chemistry using the approach detailed elsewhere (Anczkiewicz et al. 2004) and Hf isotopic (^{176}Hf/^{177}Hf) analyses with a *Neptune* MC-ICP-MS (Thermo), housed at CGS.

Oxygen isotopic analyses were performed at the University of Göttingen using laser fluorination technique combined with mass spectrometry (Thermo *MAT 253*) using analytical methods detailed elsewhere (Pack et al. 2016) with the external reproducibility on δ^{18}O values of ± 0.17 ‰ (1SD).

The U–Pb zircon geochronology was carried out at the CGS using Analyte Excite 193 nm excimer laser system (Photon Machines) connected to an *Agilent 7900* quadrupole ICP-MS and analytical conditions detailed in Soejono et al. (2024). Zircon reference samples 91,500 (Wiedenbeck et al. 1995), GJ-1 (Jackson et al. 2004), and Plešovice (Sláma et al. 2008) analysed during this study yielded concordia ages of 1063 ± 3 Ma, 603.3 ± 2.8 Ma and 338.2 ± 1.7 Ma (2σ), respectively. The raw data were processed with the

Iolite software (Paton et al. 2011) and only analyses with less than 5% discordance were used for the interpretations based on $^{206}Pb/^{238}U$ age and plotted using the Isoplot 4 toolbox (Ludwig 2008). Discordance (%) of the studied samples was calculated as follows $D = [1 - (^{206}Pb/^{238}U\ Age) / (^{207}Pb/^{235}U\ Age)] \times 100$ (Sláma et al. 2011).

The Re–Os molybdenite dating followed the protocol described in detail by Selby and Creaser (2004) that involved decomposition of a sample in a Carius tube with mixed ^{185}Re–^{190}Os–^{188}Os spike (Markey et al. 2007), Re and Os separation using solvent extraction of Cohen and Walters (1996) and anion exchange chromatography followed by isotopic measurements using a *Triton Plus* (Thermo) in negative mode (N-TIMS).

The concentrations of highly siderophile elements (Os, Ir, Ru, Pd, Pt) and Re–Os isotopic data were obtained at the joint laboratory of IG CAS (chemistry, ICP-MS) and CGS (TIMS) following the methods detailed elsewhere (e.g., Mundl et al. 2016). Osmium was separated using solvent extraction (Cohen and Waters 1996) followed by microdistillation (Nakanishi et al. 2019) and isotopic analyses ($^{187}Os/^{188}Os$) using N-TIMS technique and Thermo *Triton Plus*. Rhenium, Ir, Ru, Pt, and Pd were isolated by ion-exchange chromatography and then analyzed at IG CAS with an *Element 2* HR-ICP-MS (Thermo) coupled with an Aridus II desolvating nebulizer.

Results

Petrography, ore textures and mineral compositions

Dunite (Fig. 2a) is composed of olivine (> 90 vol%) accompanied by variable amounts of amphibole, rare clinopyroxene, and accessory spinel enclosed in a highly serpentinized matrix (Fig. 3a). Olivine forms large (up to 4 mm in diameter) grains with rather homogenous compositions (Fo ~ 82.2–85.6), but low NiO contents sometimes below detection limit (< 0.11 wt. %; Supplementary Table 2). Two different amphibole generations were recognized: **Amp I** forming irregular, large (up to 1 mm in diameter) grains that usually intergrown with olivine indicating their textural equilibrium, and **Amp II** forming small, interstitial grains (up to 300 µm in diameter) set in a serpentinized matrix. While both types belong to the calcic subgroup, **Amp I** has a pargasitic composition (Fig. 4a) (Mg# 80.8–83.2, where $Mg\# = 100 \times [Mg/(Mg + Fe_T)]$ and $Na + K > 0.5$ apfu), whereas **Amp II** mainly corresponds to magnesiohornblende (Fig. 4b) (Mg# 81.6–89.3, $Na + K < 0.5$ apfu), according to the classification of Leake et al. (1997). Accessory spinel occurs as irregular, euhedral, or rounded grains up to 1.5 mm large enclosed either in olivine/amphibole or dispersed in a serpentinized matrix (Fig. 3a). It has a highly variable composition covering a wide range of negatively correlated Cr# (Cr/[Cr + Al]) and Mg# values (Fig. 4c). Rare clinopyroxene was found only in sample RAN-18, where it forms large (up to 2 mm in diameter) grains enclosing partially serpentinized olivine. Some dunite samples (e.g., RAN-19, RAN-28) are largely affected by rodingitization reflected by the presence of garnet (grossular) + carbonate (calcite) + chlorite (Fig. 3b).

Troctolite contains variable proportions of olivine and plagioclase (up to 90 vol% in total) accompanied by minor clinopyroxene, amphibole, and accessory spinel (Fig. 3c, d). Two different rock textures were identified: (i) *protogranular* where olivine and plagioclase occur as up to 4 mm large grains of similar size whereas small clinopyroxene and amphibole grains (up to 0.5 mm) represent an interstitial phase (e.g., RAN-15), and (ii) *cumulate* characterized by up to 5 mm large plagioclase grains surrounded by smaller (< 2 mm in diameter) interstitial olivine, clinopyroxene and amphibole (e.g., RAN-16; Fig. 3c). Plagioclase with composition of anorthite ($An_{89–100}$; Fig. 4d) and elevated FeO contents (up to 0.32 wt%) displays a weak and non-systematic zonation (Supplementary Table 2). Olivine has on average lower Fo values (81.9–85.0) compared to that in dunite (Fig. 4e). Clinopyroxene with variable Cr_2O_3 contents (0.39–1.03 wt%) and Mg# values (85.0–87.5) has a composition of diopside with uniform En–Fs–Wo proportions (Fig. 4f). Amphibole that occurs in the matrix (**Amp I**) or replaces clinopyroxene (**Amp II**) (Fig. 3c, d) is predominantly calcic (magnesiohornblende to tschermakite) with Mg# of 78.8–85.1 (Fig. 4b). Spinel occurs in the form of large (up to 1.5 mm) Al-rich (hercynite) grains that enclose Cr-spinel (Fig. 3d) with highly variable Cr# (36.6–67.4); the latter is also present as isolated, up to 200 µm large grains dispersed in the matrix.

Olivine–amphibole gabbro (Fig. 2b) to gabbronorite is characterized by variable proportions of clinopyroxene and plagioclase accompanied by up to ~ 20 vol% of olivine and amphibole (**Amp I**) with grain size typically ranging from 1 to 3 mm. In some samples, common orthopyroxene is also found. Olivine usually exhibits the lowest Fo values (77.1–81.8) and NiO (< 0.11 wt%) relative to that found in other lithological types (Fig. 4e). Except of sample RAN-11, abundant orthopyroxene (enstatite with Mg# ~ 78.5–82.1) forms up to 1.5 mm large grains or ~ 200 µm thick rims along plagioclase or clinopyroxene (Fig. 3e, f). Alteration is characterized by the formation of chlorite and secondary amphibole (**Amp II**) replacing clinopyroxene. Clinopyroxene with a composition of augite to diopside (Fig. 4f) exhibits highly variable Mg# values and Cr_2O_3 contents (Supplementary Table 2). Plagioclase with elevated FeO contents (up to 0.51 wt%) has a composition of anorthite–bytownite (Fig. 4d) and some grains show a weak zonation with An-enriched rims (Supplementary Table 2). Note that plagioclase is partially

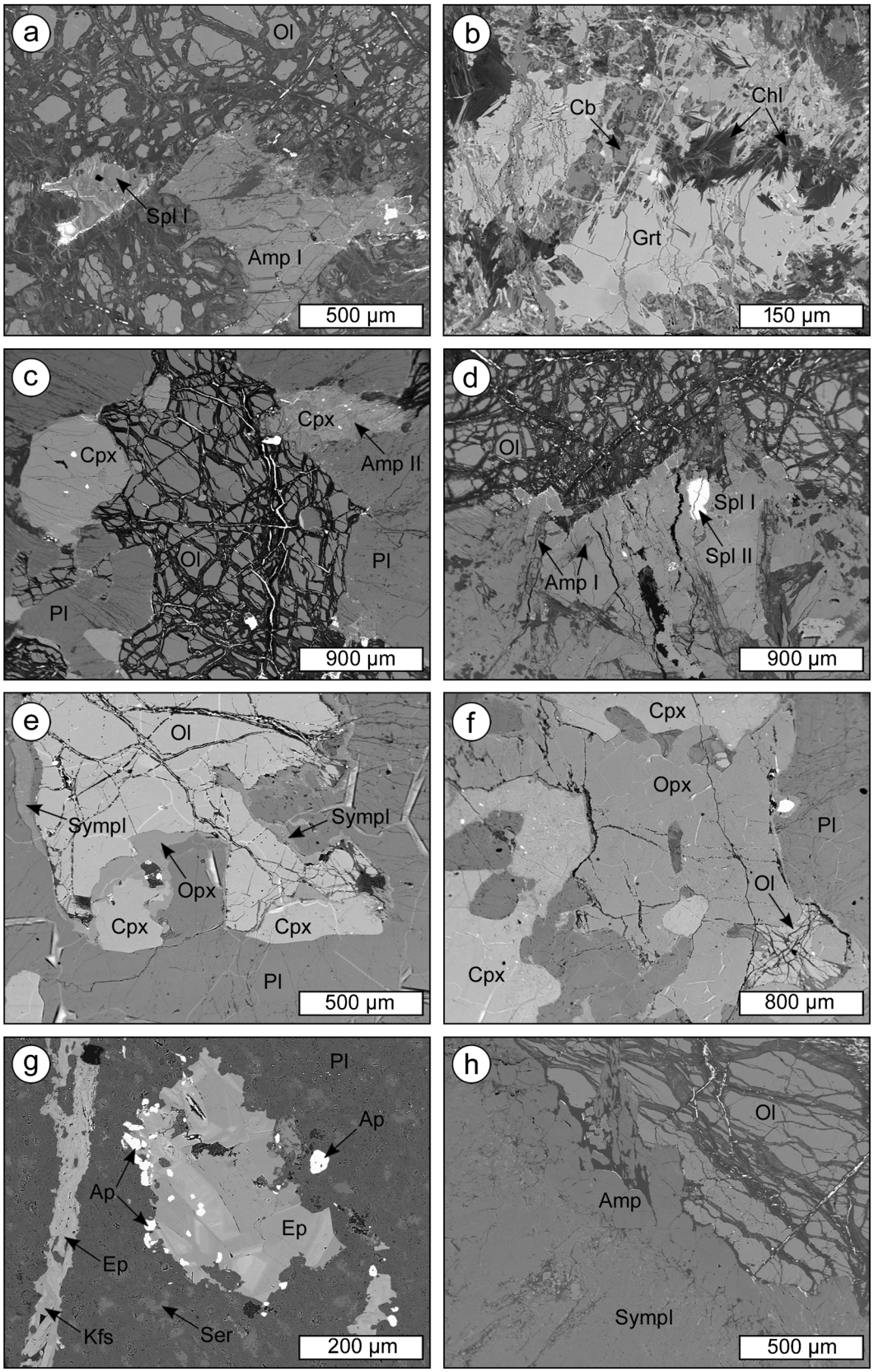
a
Ol
Spl I
Amp I
500 µm
b
Cb
Chl
Grt
150 µm
c
Cpx
Cpx
Amp II
Ol
Pl
Pl
900 µm
d
Ol
Spl I
Spl II
Amp I
900 µm
e
Ol
Sympl
Sympl
Opx
Cpx
Cpx
Pl
500 µm
f
Cpx
Opx
Pl
Ol
Cpx
800 µm
g
Pl
Ap
Ap
Ep
Ep
Kfs
Ser
200 µm
h
Ol
Amp
Sympl
500 µm

◂**Fig. 3** BSE images of major lithological types. (**a**) Dunite matrix composed of prevailing olivine, minor amphibole, and spinel. (**b**) Late-stage rodingitization of dunite reflected by the presence of hydrothermally-derived grossular, carbonate, and chlorite. (**c**) Cumulate texture of troctolite consisting of interstitial olivine around plagioclase enclosing clinopyroxene grains often replaced by amphibole. (**d**) Intergrowths of amphibole and large hercynite (Spl I) grains enclosing a crystal of Cr-rich spinel (Spl I) in troctolite. (**e**) Thin orthopyroxene rim surrounding clinopyroxene in gabbro. Note that plagioclase is marginally replaced by fine-grained symplectite composed of amphibole and spinel. (**f**) Gabbro matrix formed by plagioclase, clinopyroxene, and large orthopyroxene enclosing olivine. (**g**) Secondary epidote, apatite, and sericite typically associated with late-stage veinlets crosscutting anorthosite. (**h**) Complete breakdown of plagioclase to amphibole-spinel symplectite surrounded by thick amphibole rim and abundant olivine in metatroctolite. Abbreviations: Ol = olivine; Amp I = primary amphibole; Amp II = secondary amphibole; Spl I = Al-rich spinel; Spl II = Cr-rich spinel; Cpx = clinopyroxene; Opx = orthopyroxene; Pl = plagioclase; Grt = garnet; Cb = carbonate; Chl = chlorite; Sympl = Amp + Spl symplectite; Ep = epidote; Ap = apatite; Kfs = K-feldspar; Ser = sericite

replaced by fine-grained symplectite consisting of spinel and amphibole at the interface with neighboring minerals (Fig. 3e). Both amphibole generations (**Amp I** and **II**) have overlapping composition of magnesiohornblende–tremolite–tschermakite–pargasite (Fig. 4a, b) characterized by highly variable alkali contents and Mg# values (68.4–91.2). Spinel yields heterogeneous composition with Cr# values ranging from < 1 to 59.1 (Supplementary Table 2).

Anorthosite is represented by dykes or streaks within gabbroic lithologies (Fig. 2b). This fine-grained rock (grain size up to ~ 200 µm) is composed of plagioclase with composition of andesine (Fig. 4d) that is largely replaced by late clinozoisite. Additionally, it is crosscut by late-stage veinlets or contains isolated pockets with mineral association of prehnite + oligoclase + K-feldspar ± epidote ± sericite ± apatite (Fig. 3g). Accessory zircon forming up to ~ 40 µm rounded to euhedral grains enclosing U-rich thorite inclusions (< 5 µm) is dispersed in the matrix.

Sample RAN-30 is exceptional being mainly composed of olivine and symplectitic amphibole–spinel assemblage (Fig. 3h) formed by a breakdown of primary plagioclase (therefore, hereafter termed metatroctolite; Fig. 3e). Fine-grained amphibole–spinel symplectite forms large (up to 4 mm in diameter) grains surrounded by up to ~ 300 µm thick rims of amphibole (Fig. 3h) typically having higher Mg# (up to 91.5) compared to symplectitic amphibole (Mg# ~ 86). Olivine has relatively uniform Mg# (83.1–84.2). Spinel forms irregular, euhedral, or rounded grains of variable sizes (~ 0.1–0.8 mm) and compositions with Mg# and Cr# varying between 19.1–68.9 and 5.0–53.5, respectively.

Two studied xenoliths are essentially leucocratic rocks. Sample RAN-24 has a composition of syenite with predominant K-feldspar forming either up to 2 mm large grains with common perthitic texture or being present together with minor plagioclase and quartz in a rather fine-grained (< ~ 500 µm) matrix. In comparison, RAN-27 is a (meta) granite with a recrystallized texture dominated by quartz (< ~ 500 µm) and plagioclase (up to 1 mm in diameter) accompanied by minor K-feldspar.

The massive, net-like textured, and disseminated Ni–Cu ores at Ransko are mostly bound to troctolite and gabbro. All ore types are composed of predominant pyrrhotite sometimes containing inclusions of corundum in massive ore (Fig. 5a) accompanied by pentlandite, chalcopyrite, and minor pyrite and cubanite that locally replaces pyrrhotite (Fig. 5a–c), altogether accounting for more than 90 vol% of ore (Pašava et al. 2003). The low-temperature ore mineral phases are represented by mackinawite and valleriite. Pentlandite also forms low-temperature exsolution lamellae in pyrrhotite (Fig. 5d,e), which sometimes exhibits a so-called „bird´s-eye " texture in response to late-stage pyritization (Fig. 5e). Furthermore, Pašava et al. (2003) and Vavřín and Frýda (1998) identified Pd–Bi–Te and Pt–As platinum-group minerals (PGM) in addition to native bismuth, tsumoite, hessite, altaite, unnamed Bi–Ni telluride, and cobaltite–gersdorffite. The PGM are represented by michenerite–froodite (Fig. 5f) and sperrylite (Fig. 5g) forming small (< 50 µm in diameter) predominantly monomineralic grains dispersed in massive as well as disseminated Ni–Cu ores.

The Zn–Cu–Ba massive ore from the Obrázek deposit is characterized by the presence of sphalerite and baryte with the former commonly replaced by pyrrhotite and/or intergrown with idiomorphic pyrite (Fig. 5h). These minerals are locally associated with chalcopyrite and rare molybdenite (Fig. 5i).

Sm–Nd, U–Pb and Re–Os geochronology

Due to the absence of any U-bearing mineral phases in gabbros, seven mineral separates (amphibole, plagioclase, pyroxene) and three corresponding bulk rock gabbros (RAN-31 to 33) were analyzed for their Sm–Nd isotopic composition (Table 1) in an attempt to provide potentially reliable information on the age of gabbro. With the exception of sample RAN-32 that yields plagioclase–amphibole–bulk rock isochron age of 346 ± 29 Ma (Fig. 6), it appears that bulk rock Sm–Nd systematics has been modified by late-stage alteration considering a non-isochronous relationship with corresponding mineral phases. However, when only mineral separates from all three samples have been considered, the analyzed gabbros yielded an age of 339 ± 16 Ma (Fig. 6) that is indistinguishable within the error from mineral–bulk rock RAN-32 isochron as well as the previously obtained Re–Os age of 341.5 ± 7.9 Ma (Ackerman et al. 2013).

Granite porphyry (RAN-37) contains various zircon populations (67 concordant analyses) forming three distinct age groups with specific textural and Th/U ratio features

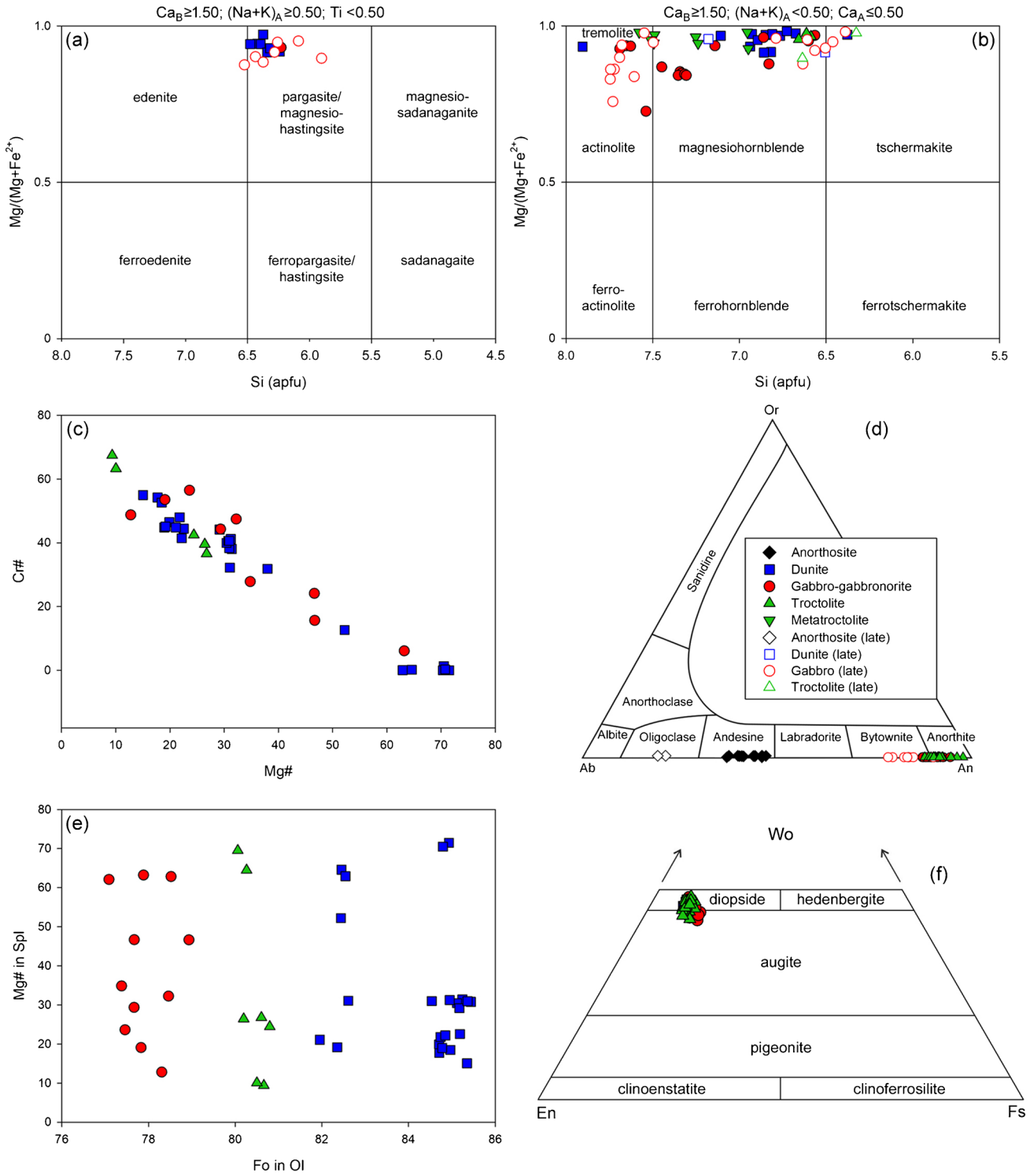

Fig. 4 (**a**, **b**) Classification diagram of amphiboles following the scheme of Leake et al. (1997). (**c**) Binary plot Mg# vs. Cr# showing compositional variations in spinel. (**d**) Ab–Or–An triangle diagram for feldspar. (**e**) Fo in olivine vs. Mg# in spinel diagram. (**f**) En–Wo–Fs classification plot for pyroxenes (Morimoto 1988). Open symbols represent late-stage phases (amphibole, plagioclase), occurring either as veinlets (anorthosite) or alteration products (dunite–troctolite–gabbro) after primary mineral assemblages

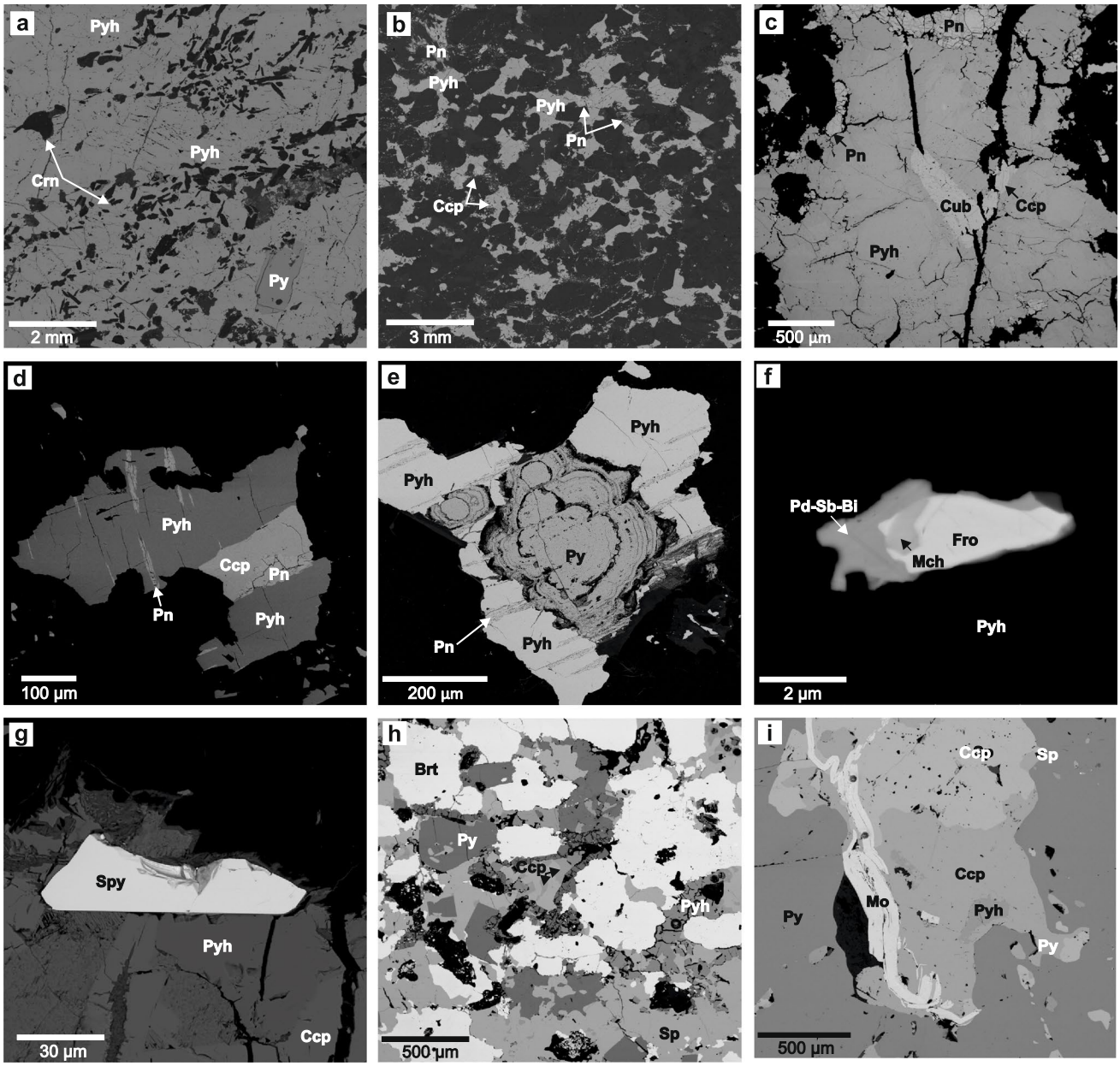

Fig. 5 Back-scattered electron (BSE) images of mineralized samples from the Ni–Cu and Zn–Cu–Ba ores at Ransko. (**a**) massive texture dominated by pyrrhotite (Pyh) and locally with pyrite (Py) and corundum (Crn), Jezírka Ni–Cu deposit. (**b**) net-textured sulfides (pyrrhotite-Pyh, pentlandite-Pn, and chalcopyrite-Ccp) in troctolite, Jezírka Ni–Cu deposit. (**c**) major sulfides represented by pyrrhotite (Pyh) intergrowing with pentlandite (Pn), chalcopyrite (Ccp), and cubanite (Cub), Jezírka Ni–Cu deposit. (**d**) low-temperature segregations of pentlandite (Pn) in pyrrhotite intergrowing with chalcopyrite (Ccp), Jezírka Ni–Cu deposit. (**e**) typical „bird´s-eye " structure related to pyritization (Py) of pyrrhotite (Pyh) in altered gabbro, Jezírka Ni–Cu deposit. (**f**) a new Pd–Sb–Bi phase in association with michenerite (Mch) and froodite (Fro), Jezírka Ni–Cu deposit. (**g**) sperrylite associated with pyrrhotite (Pyh) and chalcopyrite (Ccp), Jezírka Ni–Cu deposit. (**h**) dominant baryte (Brt) and sphalerite (Sp) accompanied by pyrrhotite (Pyh), chalcopyrite (Ccp) and pyrite (Py), Obrázek Zn–Cu–Ba deposit. (**i**) molybdenite in association with base metal sulfides, Obrázek Zn–Cu–Ba deposit

(Fig. 7, Supplementary Table 3): (1) 293.9 ± 3.5 Ma (8 grains; Fig. 7b) with dark CL appearance and Th/U values below ~ 0.07 that collectively indicate metamict nature of the zircons related to a late-stage resetting event, (2) 346.4 ± 1.7 Ma (27 grains; Fig. 7c) obtained for rounded zircons (cores) that are characterized by visible internal CL structure and Th/U ratios in the range of ~ 0.08 to 0.4, and (3) 459.7 ± 3.5 Ma (18 grains; Fig. 7d) population with oscillatory zoning and Th/U ratios from ~ 0.2 to 0.5. Additionally, three minor peaks at ca. 514, 570, and 620 Ma were detected

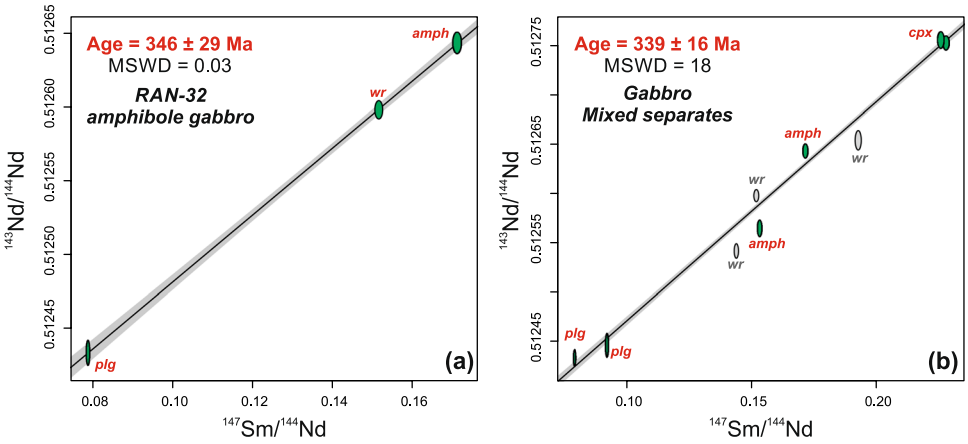

Fig. 6 Samarium–Nd isochrons for gabbroic rocks from the Ransko massif. (**a**) plagioclase–whole-rock–amphibole isochron, olivine–amphibole gabbro (sample RAN-32). (**b**) combined plagioclase–amphibole–clinopyroxene isochron (samples RAN-31, RAN-32 and RAN-33)

in zircons (cores) that show similar morphological characteristics as the third age group.

A single sample of molybdenite intimately associated with the Obrázek Zn–Cu–Ba mineralization (Fig. 5i) yielded a Re–Os age of 343.7 ± 1.7 Ma (Supplementary Table 4).

Bulk rock major and trace element compositions

The Ransko (ultra)mafic rocks have essentially tholeiitic composition that is expressed by very low alkali contents ($Na_2O + K_2O < 1$ wt%, except sample RAN-12; Fig. 8a,b; Supplementary Table 5). When samples containing high proportion of sulfides (> 4 wt% S) are excluded, the troctolites plot within the field of peridotitic gabbro in the TAS diagram (Middlemost 1994) while slightly more alkaline gabbros fall into a compositional field of peridotitic gabbro to gabbro (Fig. 8a). In comparison, two anorthosite samples plot in the field of monzonite due to their high Na_2O contents (5.9 and 6.8 wt%). Finally, two leucocratic xenoliths have a composition of syenite (RAN-24) and granite (RAN-27) in the TAS diagram, in agreement with their petrography (see above).

Selected major elements display notable correlations with SiO_2 (Fig. 8c-f) that illustrate large compositional variations of the Ransko (ultra)mafic rocks controlled by the variable proportions of olivine, pyroxenes, plagioclase, and amphibole. Thus, dunites are characterized by uniformly low SiO_2, but very high MgO contents among the studied rocks (Fig. 8d) whereas gabbro–gabbronorite samples exhibit a wide range of Al_2O_3, MgO, and CaO contents at a given SiO_2 value (Fig. 8c–e). Overall, all studied rocks yield very low TiO_2 contents (< 0.11 wt%) and variable CO_2 values with the highest values (> 0.34 wt%) detected in dunites RAN-18 and 21 that experienced rodingitization. Concentrations of minor elements (Sc, V, Cr, Zn) generally decrease with increasing SiO_2 values (not shown) indicating their control by parental melt evolution while the distribution of Ni and Cu is largely controlled by the variable presence of Ni–Cu sulfides.

Rare earth element (REE) and extended trace element distributions normalized to chondrite (Boynton 1984) and N-MORB (Sun and McDonough 1989), respectively are plotted in Fig. 9. Overall, dunites, troctolites and gabbro–gabbronorites display mostly similar REE patterns characterized by mild enrichment of LREE with respect to HREE ($La_N/Yb_N = 1.1–4.6$) and variably positive Eu anomalies ($Eu_N/Eu^* = 1.0–4.0$; $Eu^* = \sqrt{(Gd_N \times Sm_N)}$). In contrast, anorthosites are characterized by U-shaped patterns (La_N/Sm_N of 12 and 37, Tb_N/Lu_N of 0.15 and 0.41) because of the presence of apatite and zircon, respectively. Two xenoliths display U-shaped REE distributions (La_N/Sm_N of ~ 2.9) and pronounced negative Eu anomaly (Eu/Eu* of 0.3–0.4). The Ransko (ultra)mafic rocks collectively exhibit selective enrichments in some large ion lithophile elements (LILE; e.g., Cs, Rb, Ba), pronounced negative Nb anomaly ($Nb_N/La_N = 0.02$ to 0.3) and largely positive Pb anomaly that is paralleled by variable but positive Sr anomaly (Fig. 9) reflecting plagioclase accumulation. Additionally, anorthosites have marked positive Th–U anomaly due to the presence of zircon that commonly encloses thorite.

The Ransko rocks with high proportions of Ni–Cu ores (samples RAN-10, RAN-17, RAN-34, and RAN-35) are characterized by variable Ni and Cu contents that reach up to ~ 0.5 and 3 wt%, respectively. The highest Co content was detected in sample RAN-34 (1190 ppm Co; Supplementary Table 5). By contrast, Zn–Cu ores (samples RAN-22 and RAN-23) contain up to ~ 13 and ~ 0.5 wt% Zn and Cu, respectively, while the low totals determined (< 42 wt%) for bulk-rock analyses are likely attributed to non-decomposed baryte.

Sr–Nd–Hf–Pb–O isotopic compositions

The (ultra)mafic Ransko rock types exhibit overlapping initial (340 Ma) values with $^{87}Sr/^{86}Sr_{(i)}$ between 0.7047

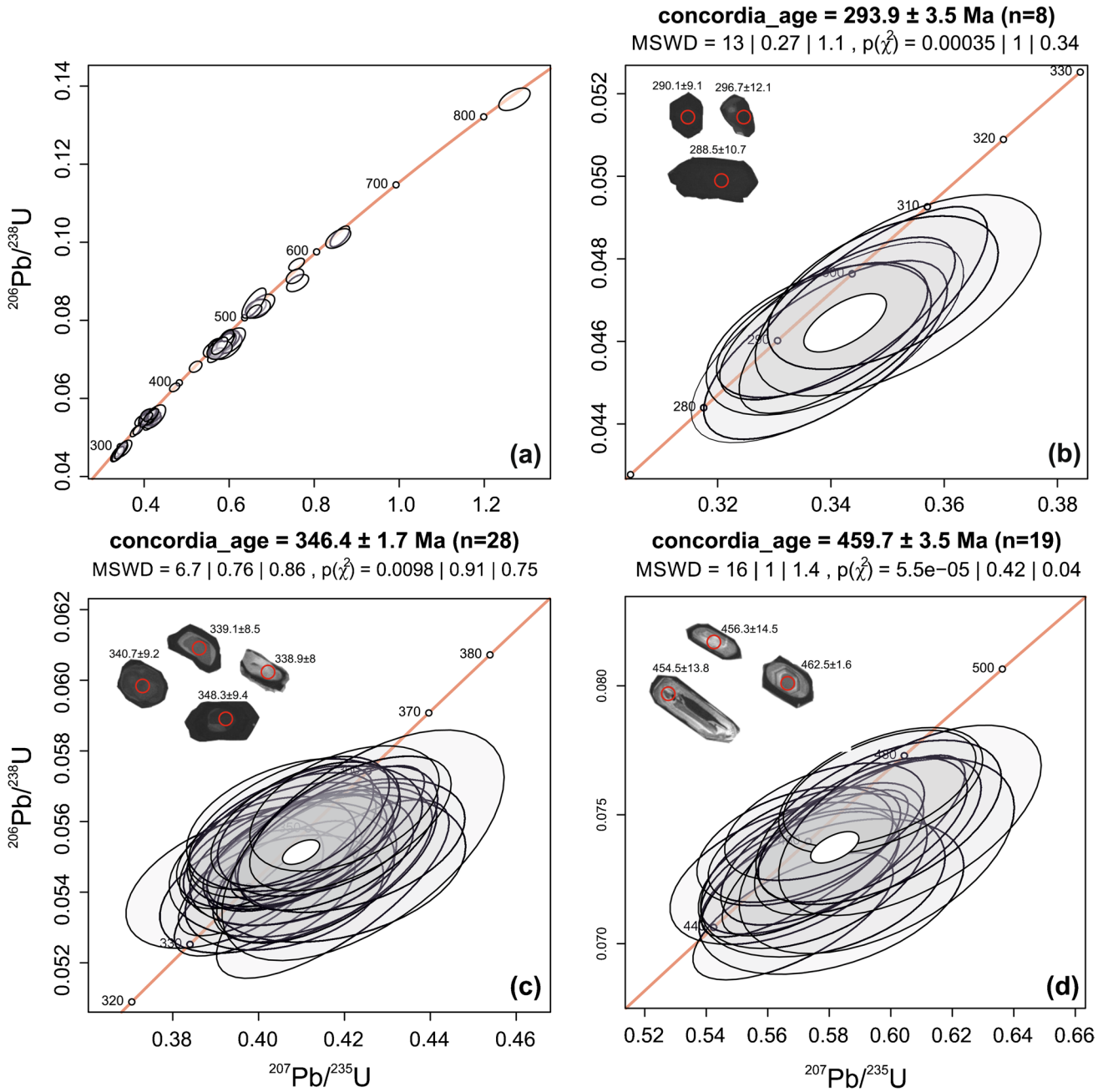

Fig. 7 The U–Pb concordia plots (**a**-**d**) for the Ransko granite porphyry (sample RAN-37) along with representative CL zircon images for three individual age groups (**b**–**d**) defined (see the text for more explanation)

and 0.7069 whereas $\varepsilon_{Nd(i)}$ vary in a rather narrow range from +0.9 to +2.7 (Fig. 10a, Table 2). The age of the two studied xenoliths is fairly uncertain, but if 340 Ma is considered (assumed for most country rocks), they have very similar $\varepsilon_{Nd(i)}$ of +0.4 and +0.8 whereas their $^{87}Sr/^{86}Sr_{(i)}$ values are distinctly different as a consequence of their contrasting $^{87}Rb/^{86}Sr$ values (Table 2). Lutetium–Hf isotopic data (Table 3) were determined only for a small subset of samples because the (ultra)mafic rocks contain very low Hf contents (Supplementary Table 5). Gabbros, troctolites, and anorthosites exhibit a limited variability in $\varepsilon_{Hf(i)}$ values from +8.2 to +11.5 with the lowest values detected in anorthosites (Fig. 10b, Table 3). Conversely, the xenoliths yield lower $\varepsilon_{Hf(i)}$ of +5.0 and +5.7. Lead isotopic compositions for the Ransko gabbro–troctolite–dunite association as well as syenite xenolith (RAN-24) yield remarkably homogeneous initial $^{206}Pb/^{204}Pb$, $^{207}Pb/^{204}Pb$ and $^{208}Pb/^{204}Pb$ values (Table 4) that plot on

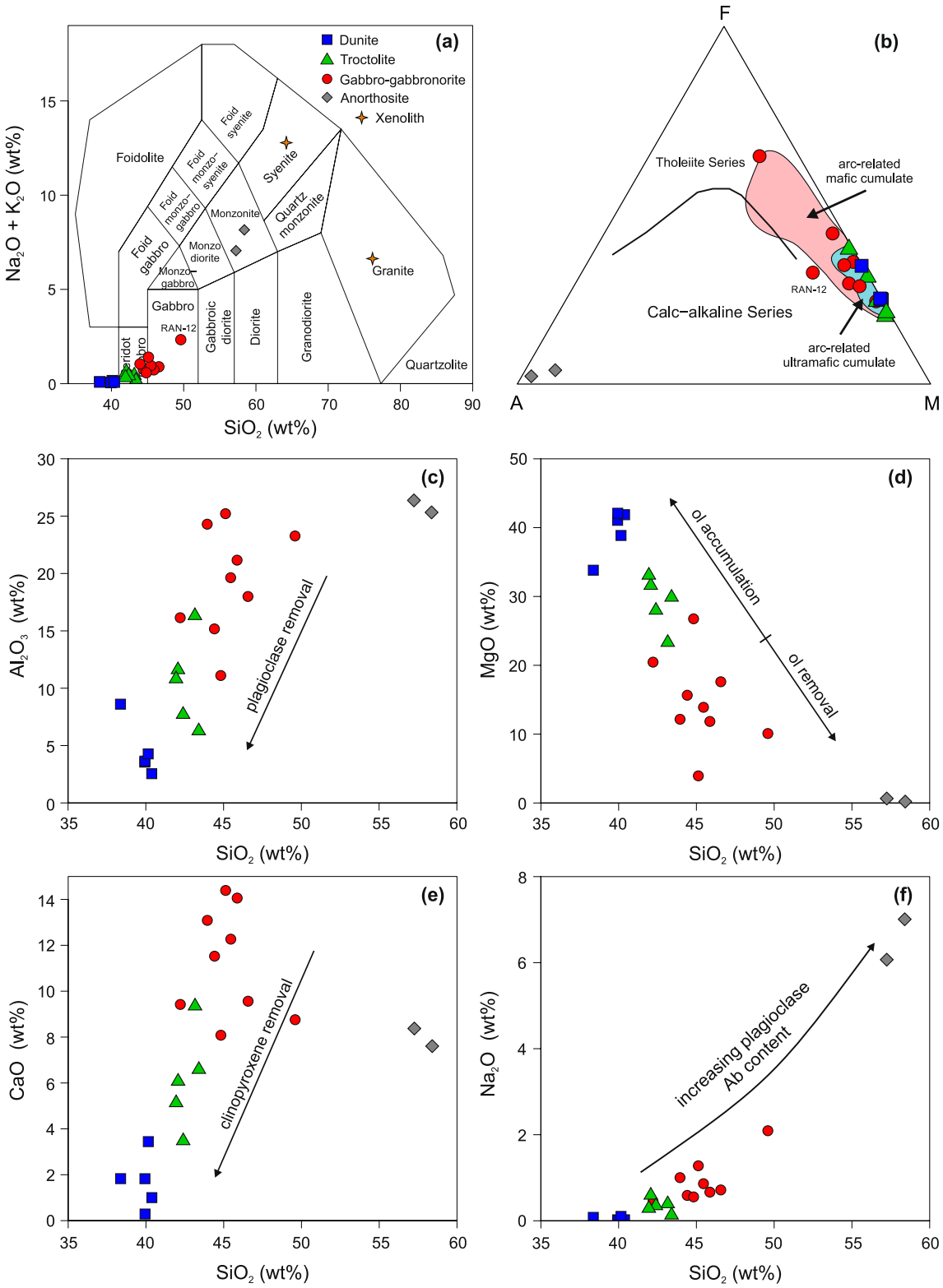

Fig. 8 Major element variations and classification diagrams for the studied Ransko (ultra)mafic rocks, anorthosite, and entrained xenoliths. (**a**) Total alkali-silica (Middlemost 1994) and (**b**) AFM (Irvine and Baragar 1971) diagrams illustrating predominantly tholeiitic compositions of the Ransko (ultra)mafic rocks (fields for arc-related cumulate rocks from Beard 1986). (**c**–**f**) Harkers variation diagrams illustrating the effect of fractional crystallization and crystal accumulation using variations between SiO_2 and selected major element oxides (Al_2O_3, MgO, CaO, Na_2O)

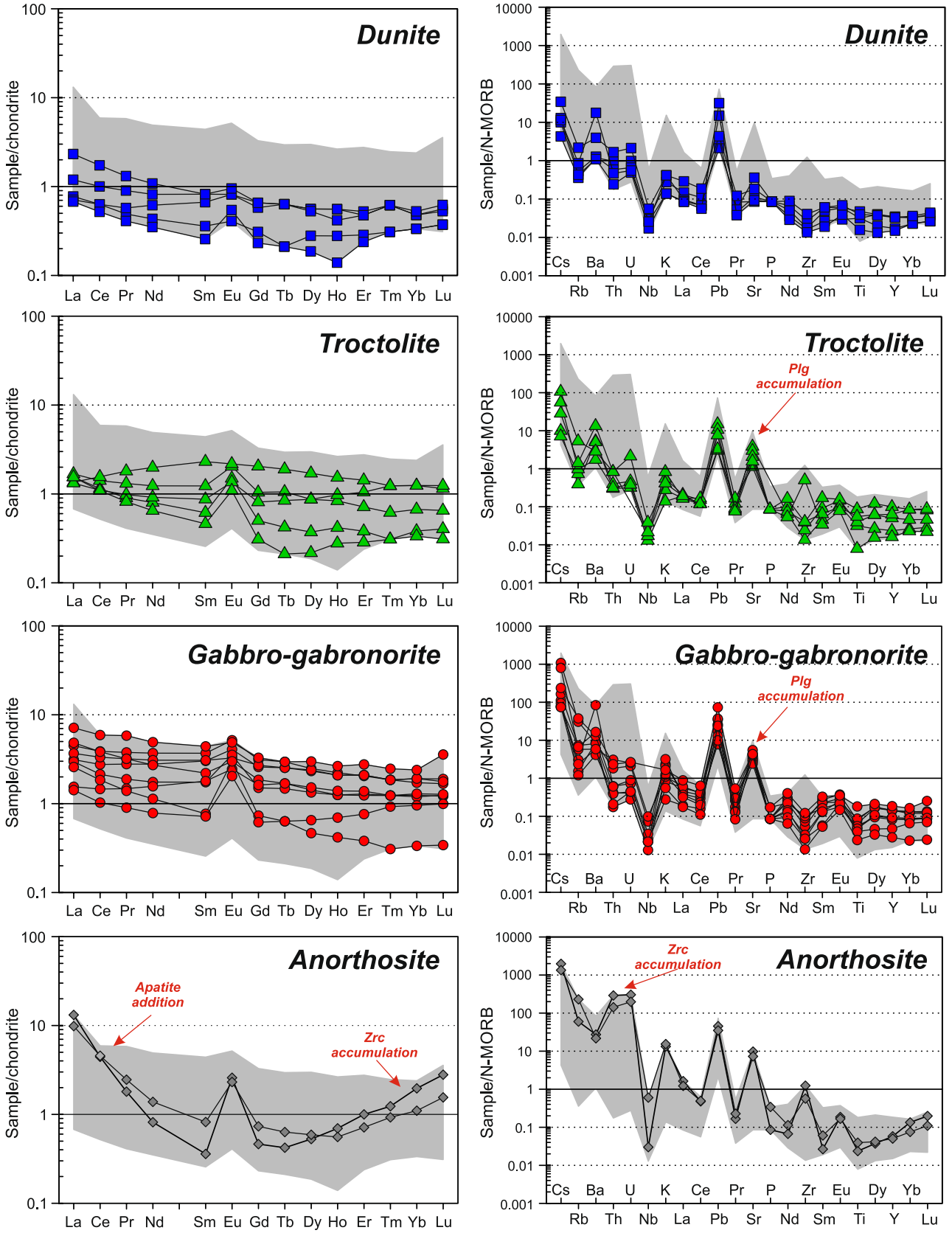

Fig. 9 Rare-earth element (REE) distributions normalized to chondrite (Boynton 1984) and trace element distributions normalized to N-MORB (Sun and McDonough 1989) for the Ransko (ultra)mafic rocks and anorthosites

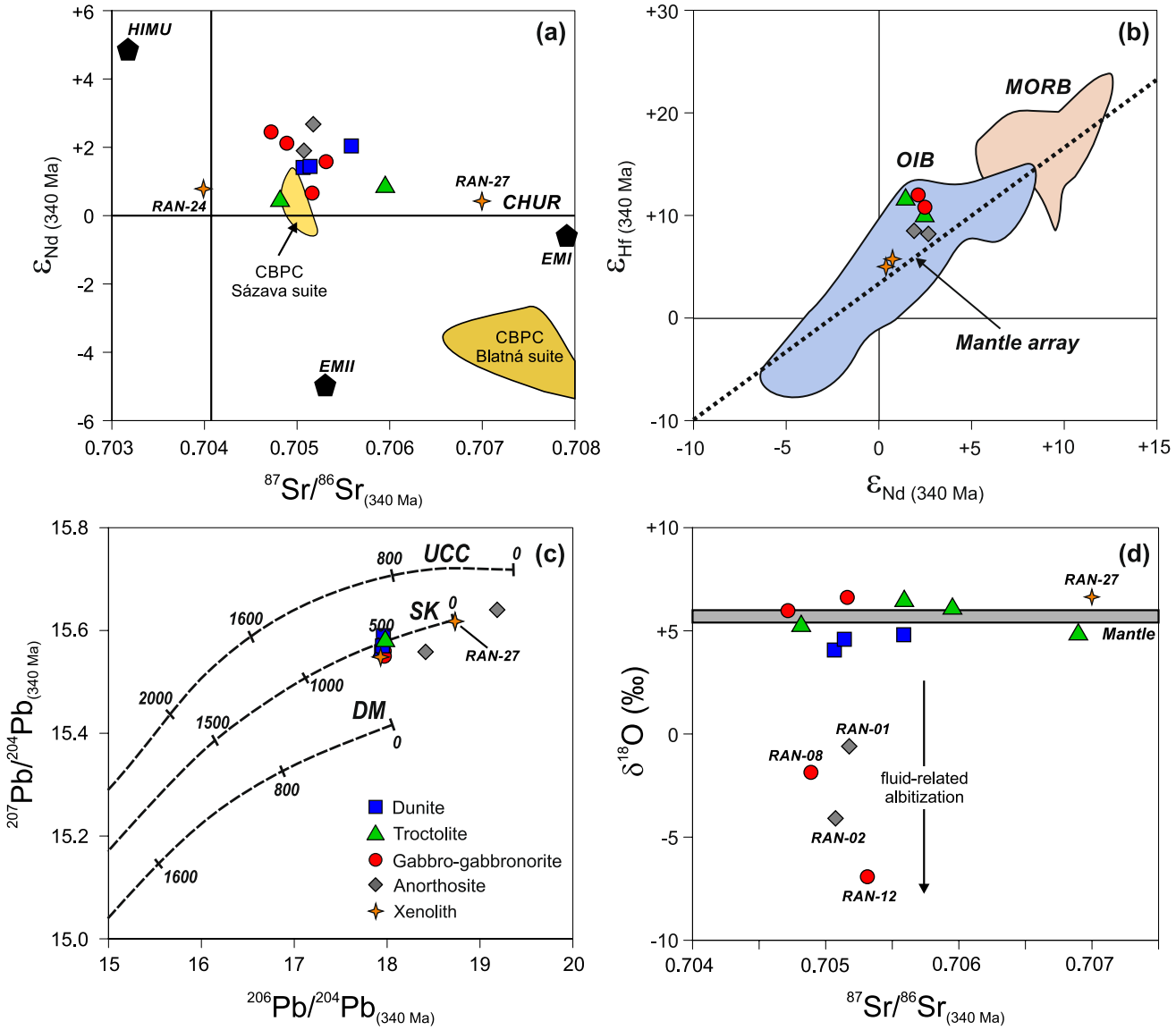

Fig. 10 Strontium–Nd–Pb–O isotopic compositions of the Ransko (ultra)mafic rocks, anorthosites, and xenoliths entrained by the massif. (**a**) Initial (340 Ma) Sr–Nd and Nd–Hf (**b**) bivariate plots. Present-day composition of mantle components DMM, EM I, EM II, and HIMU from Zindler and Hart (1986) whereas the MORB and OIB fields were constructed using the data of Salters (1996), Blichert-Toft and Albarède (1999) and Chauvel and Blichert-Toft (2001). Strontium–Nd isotopic compositions of the Sázava and Blatná suites of the CBPC are compiled from Janoušek et al. (2022) and the terrestrial Hf–Nd array is from Vervoort et al. (1999). (**c**) Initial (340 Ma) $^{207}Pb/^{204}Pb$ vs. $^{206}Pb/^{204}Pb$ diagram illustrating mildly enriched nature of the Ransko rocks. Lead evolution curves of the depleted mantle (DM), and upper continental crust (UCC) are adopted from Doe and Zartman (1979) whereas SK Pb evolution curve is from Stacey and Kramers (1975). (**d**) The $\delta^{18}O$ vs. $^{87}Sr/^{86}Sr$ plot. Note a large shift to lower $\delta^{18}O$ values in response to fluid-driven albitization. Upper mantle $\delta.^{18}O$ value from Mattey et al. (1994)

the Stacey–Kramers Pb evolution curve (Fig. 10c). In contrast, anorthosites and (meta)granite xenolith RAN-27 display more radiogenic Pb isotopic compositions due to the presence of U–Th-rich minerals (see Petrography section). The majority of the Ransko rocks exhibit $\delta^{18}O$ values that plot within or slightly below/above the $\delta^{18}O$ value estimated for Earth`s upper mantle (+5.2 ± 0.3 ‰; Mattey et al. 1994; Fig. 10d) whereas $\delta^{18}O$ values in both anorthosites and gabbros RAN-08 and RAN-12 depart to significantly lower $\delta^{18}O$ values (as low as − 6.9 ‰ in RAN-12; Table 2).

Highly siderophile element and Re–Os isotope systematics

Barren and low-mineralized (Ni–Cu) samples are characterized by rather low iridium-group PGE (I-PGE; Os, Ir, Ru) concentrations (< 7 ppb in total) with the highest contents found in dunites whereas platinum-group PGE (P-PGE; Pt, Pd) abundances reach up to 120 and 65 ppb, respectively (Table 5), with no relationship to total sulfur contents for any HSE. In contrast, troctolites RAN-10, RAN-17, and RAN-35 with large proportions of Ni–Cu ore as well as massive Ni–Cu ores (Pašava et al. 2003; Ackerman et al. 2013) have markedly higher I-PGE values (up to ~ 90 ppb) that are partially correlated with sulfur contents (not shown). The primitive mantle-normalized HSE patterns for all studied samples show similar distributions with steep enrichments from Os to

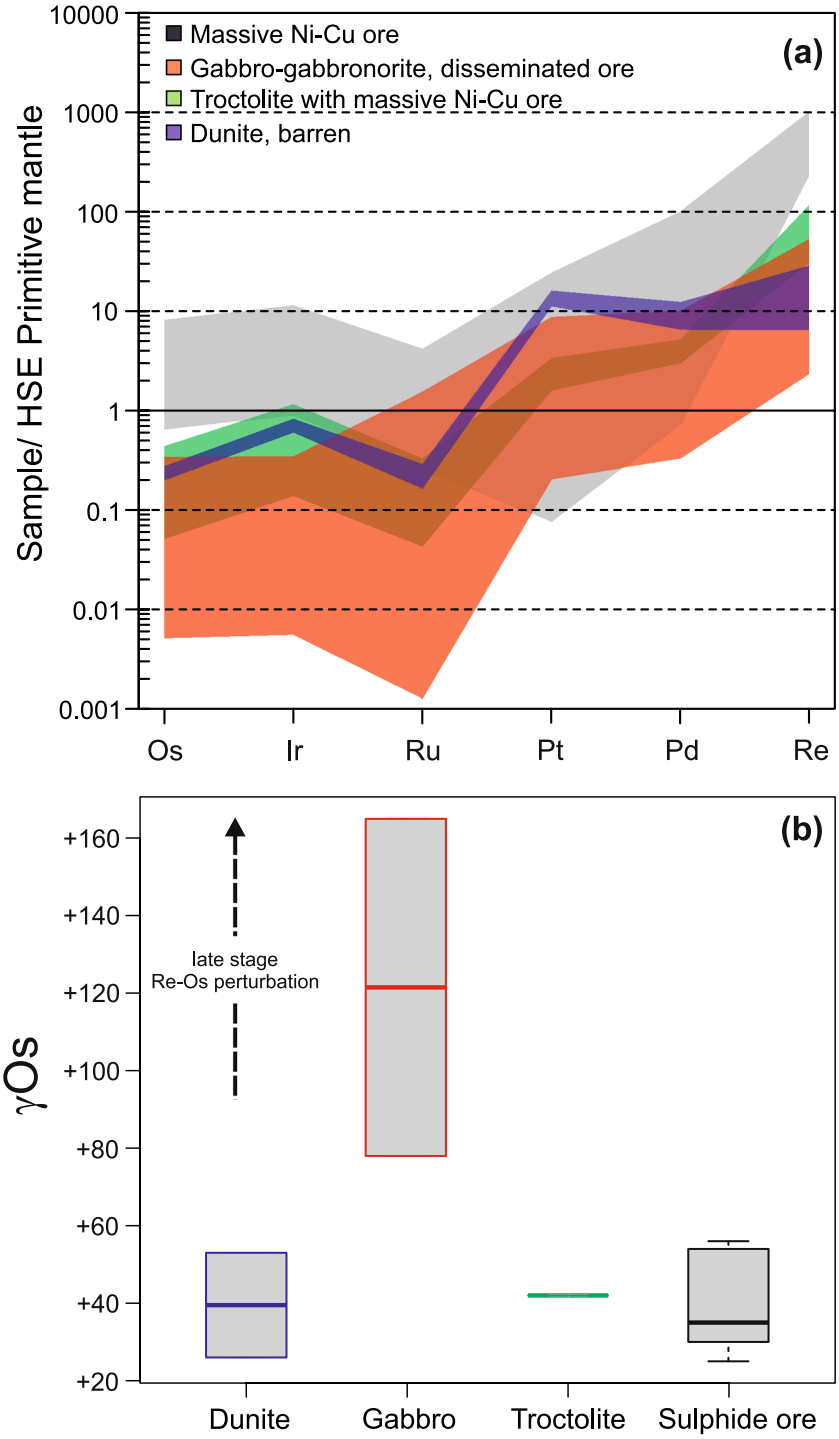

Fig. 11 Highly siderophile element and $^{187}Os/^{188}Os$ isotopic systematics of the barren and variable mineralized Ransko (ultra)mafic rocks. (**a**) Primitive mantle-normalized (Day et al. 2016) distributions of Os, Ir, Ru, Pt, Pd, and Re. (**b**) Variations in initial $^{187}Os/^{188}Os$ compositions expressed as γOs values among dunite, gabbro, troctolite, and sulfide ores

Re, sometimes with small positive Ir, but pronounced negative Ru anomalies (Fig. 11a). The Re–Os isotopic compositions expressed by the initial γOs values (back-calculated to 340 Ma) exhibit a rather low degree of variation for dunite, troctolite, and Ni–Cu ores (+25 to +77; Fig. 11b). Predominantly negative γOs values have been calculated for gabbros and anorthosites suggesting late-stage perturbation of Re–Os systematics (Fig. 11b).

Discussion

Constraints on the age of the ransko massif and timing of Zn–Cu–Ba mineralization

The exact timing of magmatic activity in the Ransko massif has remained a matter of debate for a long time (Marek 1970; Mísař 1974; Pašava et al. 2003; Ackerman et al. 2013). The previously assumed lower Cambrian age (Marek 1970) has been questioned not only by Re–Os geochronology yielding an age of ~ 342 Ma (Ackerman et al. 2013), but also by field observations providing evidence for the presence of pre-Variscan rocks, such as xenoliths within Ransko (ultra) mafic lithologies (V. Kachlík, pers. comm).

Our new geochronological data on gabbros (Sm–Nd) as well as granite porphyry (U–Pb) further underscore the Variscan age of the Ransko massif (Figs. 6 and 7). First, despite somewhat larger age uncertainty, mixed mineral separates as well as plagioclase–amphibole–whole rock isochrons for gabbro yield the overlapping Sm–Nd ages of 339 ± 16 Ma and 346 ± 29 Ma (Fig. 6a, b), respectively. Second, the U–Pb zircon age of granite porphyry forming a dyke swarm crosscutting the Ransko massif, thereby bracketing the lower age limit of the massif, yields a prominent age cluster at 346.4 ± 1.7 Ma (Fig. 7c). This can be best interpreted as magmatic crystallization age while the variable but older zircon ages (> 459 Ma) plausibly represent inherited ages related to the surrounding geological units (Fig. 7d). Therefore, considering all errors associated with the individual methods used, in combination with available geochronological data for the surrounding, closely related units and field observations, these lines of evidence implicate an emplacement of the Ransko massif during the Variscan orogenesis between ~ 370 and 345 Ma. Such a constrained age remarkably overlaps with the gamut of geochronological data already collected for syn-convergent arc-related large bodies of calc-alkaline I-type granitoids present along the margin between Teplá–Barrandian and Moldanubian units (~ 375–373 Ma; Žák et al. 2011; Venera et al. 2000), CBPC (~ 360–347 Ma; Janoušek et al. 2004), ~ 346 Ma for the nearby calc-alkaline Miřetín Pluton (Vondrovic et al. 2011) and ~ 341 Ma Nasavrky Plutonic Complex (Re–Os molybdenite; Ackerman et al. 2017). Therefore, this indicates a significant subduction-related magmatic event with coeval acidic and (ultra)mafic magmatic activity between ~ 360 and 345 Ma that will be further explored below.

The obtained Re–Os age of ~ 344 Ma obtained for Zn–Cu–Ba mineralization (Supplementary Table 5) overlaps with the Re–Os age of Ni–Cu mineralization as well as U–Pb zircon age obtained for porphyry dykes. Therefore, this confirms earlier assumptions that epigenetic Zn–Cu–Ba ores were emplaced in a close genetic relationship with late-stage intrusions of quartz diorite and associated hydrothermal activity soon after the consolidation of (ultra)mafic Ransko rocks (Mísař 1974 and references therein) and further highlights the importance of Variscan-related processes for the Ransko metallogenesis.

Geotectonic settings and petrogenesis

The Ransko massif exhibits several lines of evidence for its predominantly cumulate origin and, therefore, an important role of fractional crystallization and crystal accumulation. First, the rocks are essentially (ultra)mafic with highly variable proportions of olivine, amphibole, clinopyroxene, and plagioclase while most of them show characteristic cumulate textures, that are especially apparent in the case of troctolites and dunites with the cumulus plagioclase in the latter and intercumulus olivine in the former (e.g., Fig. 3c). Second, except a single sample of olivine–amphibole gabbro RAN-12 that has a high content of plagioclase, the rocks exhibit largely tholeiitic composition (Fig. 9a, b) characterized by very low alkali contents ($Na_2O + K_2O < 1$ wt%) along with overall high bulk-rock Mg# values and Fo contents in olivine, both increasing from gabbro (Mg# = 75–85, Fo of 77–82) to troctolite/dunite (Mg# = 80–92, Fo of 82–85; Fig. 5e). Considering the common presence of amphibole-bearing troctolites and dunites accompanied by subordinate anorthosites and largely decreasing CaO contents in gabbros at a given SiO_2, this highlights the importance of clinopyroxene crystallization. At the same time, important, but variable olivine, plagioclase ± amphibole crystal accumulation is demonstrated by the modal compositions, overall very high MgO contents (Fig. 8c), generally increasing An values of plagioclase from gabbro to troctolite (Fig. 4d; Supplementary Table 2) and well-recognized positive Sr and Eu anomalies (Fig. 10). In comparison, anorthosites are characterized by the presence and accumulation of zircon–thorite, expressed by notable U–Th and HREE enrichments (Fig. 9).

As noted above, the ~ 370–345 Ma emplacement age of the Ransko massif markedly overlaps with arc-related magmatic activity recorded by CBPC and Nasavrky granitic complexes where the latter is situated in the northern periphery of Ransko (Fig. 1b). Considering the very similar Sr–Nd isotopic compositions of the Ransko rocks with the most primitive member of CBPC (Sázava suite; Fig. 10a),

it might be possible that the Ransko magma was intimately connected with those parental to CBPC and Nasavrky suites. To test this hypothesis, we performed a single-stage fractional crystallization modelling using whole-rock REE compositions and distribution coefficient for mafic to intermediate magmas (see Supplementary Table 6). In this model, the most primitive member of the CBPC (Sázava suite) serves as a melt that originated through melting of some hypothetical, arc-related lower crustal metabasic rocks (Janoušek et al. 2000), while the Ransko (ultra)mafic rocks may represent the associated crystal cumulate lithologies. Several compositions that might be representative of parental melt compositions (Supplementary Table 6) as well as different mass fractions removed or proportions of crystalizing mineral assemblage that consists of olivine, clinopyroxene, amphibole, and plagioclase were tested. Nonetheless, using this approach, we were not able to reproduce the very low REE contents and flat distributions of the Ransko (ultra) mafic rocks. This might be related to either more complex processes that involve, for example, magmatic mixing/mingling and assimilation of continental crust documented for the CBPC (Janoušek et al. 2000, 2004) or the different compositions of the Ransko parental melt. We suggest the latter possibility as more plausible considering more radiogenic Nd–Hf–Pb isotopic systematics and notably tholeiitic nature of the Ransko (ultra)mafic rocks in comparison to the Sázava CBPC.

Broadly homogeneous Nd–Hf–Pb isotopic signatures across different rock types (Fig. 10) might indicate a rather limited role of crustal contamination. However, common presence of crustal xenoliths within the Ransko (ultra)mafic rocks as well as determined Sb/Se and As/Se ratios for pentlandite (Pašava et al. 2023) collectively indicate some degree of crustal assimilation, partially hindered by a similarity of Nd–Hf–Pb isotopic compositions of wall rock (e.g., samples RAN-24 and RAN-27).

Despite the extensive fractional crystallization/crystal accumulation processes that do not permit to reliable use of classification diagrams for the discrimination of Ransko geotectonic settings (e.g., Hollocher et al. 2012; Pearce 2008), its arc-related signature (geotectonic setting) is well-demonstrated by its major/trace element and isotopic composition as well as mineralogy. First, the presence of primary amphibole in all (ultra)mafic rock types (Supplementary Table 2, Fig. 5) as well as overall enrichment in LILE indicate water-rich conditions of the parental magma while the common presence of orthopyroxene in gabbros is characteristic of high fO_2 conditions (e.g., Berndt et al. 2005). This is paralleled by a pronounced negative Nb anomaly recorded in the entire Ransko suite (Fig. 9), typical for arc-related magmas (e.g., Pearce 2008; Ulmer et al. 2018). Secondly, the predominant olivine + plagioclase association together with the rather Fe-rich nature of olivine (Fig. 4e) and position of the Ransko rocks in the AFM diagram (Fig. 8b) is typical for arc-related (ultra) mafic cumulates (Beard 1986). Thirdly, possible affinity to oceanic crust source (e.g., tholeiitic character, low incompatible element contents; Fig. 9) is not supported by rather mildly radiogenic initial Hf–Nd isotopic compositions (ε_{Nd} from + 0.9 to + 2.7 and ε_{Hf} up to + 12.0) and decoupled Sr–Nd signatures (Fig. 10a,b). Together with homogeneous Pb isotopic compositions (Fig. 10c) and radiogenic γOs values (Fig. 11), all these lines of evidence indicate derivation of the Ransko parental melt from an enriched mantle source, such as metasomatized mantle wedge at convergent plate margin-related setting.

At arc-related settings, (ultra)mafic intrusions that host important Ni–Cu–PGE mineralizations are commonly represented by concentrically zoned Alaskan-type complexes (Himmelberg and Loney 1995; Johan 2002; Thakurta et al. 2008; Cui et al. 2020). However, while some characteristics of the Ransko massif (e.g., elliptical shape, ultramafic composition with large quantities of dunites, partially concentric structure) might indicate its affinity to Alaskan-type intrusions, at least two indices argue against this hypothesis. Notably, clinopyroxene-rich or hornblendite lithologies representing characteristic Alaskan-type lithological feature (Johan 2002 and references therein) are virtually absent at Ransko where orthopyroxene is common in gabbros. At the same time, the spinel Cr# < 60 (Fig. 4c) is also well below that typically reported for Alaskan-type complexes (e.g., Garuti et al. 2003).

The Ransko (ultra)mafic rocks show undisputable evidence of hydrothermal alterations involving olivine (serpentinization), pyroxene/amphibole (uralitization, chloritization) as well as plagioclase (saussuritization) in response to reactions with orthomagmatic fluids that are considered to be related to late phases of magmatic activity and/or massif solidification (e.g., Mísař 1974), in contrast to the apparently younger documented overprints (rodingitization – Fig. 3b; epidotization – Fig. 3g). Accordingly, this late-stage alteration of (ultra)mafic lithologies produces rather minor and non-systematic modifications to bulk-rock $\delta^{18}O$ values (Fig. 10d). On the other hand, it is apparent that plagioclase-rich lithologies that suffer from high degree of fluid-related albitization expressed by the formation of bytownite at the expense of anorthite (gabbro) and oligoclase after andesine (anorthosite, Fig. 4d) exhibit marked oxygen isotope exchange driving $\delta^{18}O$ values to negative values (down to − 6.9 ‰; Fig. 10d). This is likely because plagioclase is much more susceptible to oxygen isotope exchange than clinopyroxene (e.g., Fehlhaber and Bird 1991). Yet, the absence of a relationship between $\delta^{18}O$ and initial $^{87}Sr/^{86}Sr$ (not shown) indicates that this process was not responsible for the observed decoupled Sr–Nd signatures.

Origin of Ni–Cu–(PGE) mineralization

The cogenetic magmatic Ni–Cu–PGE ores (see Sect. 4.1. describing the ore textures) are spatially distributed within a rather narrow NE–SW trending zone (Fig. 1c) where they are not bound to any specific rock type. Conversely, the ore bodies are located either in gabbro or dunite (e.g., Řeka deposit) or in the zones of varied alternation of troctolite and gabbro (e.g., Jezírka deposit) in the form of irregular lenses and horizons that roughly follow the contact between gabbro and troctolite (Mísař 1974; Holub et al. 1992; Pašava et al. 2003). Furthermore, the ores are concentrated in places characterized by marked, late-stage, fluid-assisted alteration (Mísař 1974) and base metal sulfides commonly replace silicates. These observations argue for the emplacement of Ni–Cu ores during the latest stages of the magmatic activity of the Ransko massif.

The textural types of Ni–Cu–PGE ores vary from semi-massive/massive (Fig. 2c) containing > 15 wt% S (e.g., sample RAN-34) through predominantly net-like (Fig. 2d) with S contents between ~ 5 and 10 wt% characterized by the variable presence of sulfides within olivine cumulates (e.g., sample RAN-17) to disseminated textures (Fig. 2e) with low S contents (< ~ 5 wt%; e.g., samples RAN-07 and RAN-08). Such diverse textures indicate a complex emplacement style of Ni–Cu–PGE ores at Ransko that is common in many Ni–Cu deposits worldwide (e.g., Barnes et al. 2017, 2018; Mao et al. 2022; Zuccarelli et al. 2022) where the genesis of peculiar net-textured sulfides remains questioned (e.g., Hudson 1972; Naldrett 1973; Barnes et al. 2018; Mao et al. 2022). Previously, Mísař (1974) proposed a model for the formation of Ni–Cu ores at Ransko where the sulfidic melt was formed through the liquid immiscibility from the parental silicate melt and then squeezed upward during the final emplacement of the massif along suitable (tectonically or lithologically weakened) structures. However, considering more recent observations of Ni–Cu occurrences at a global scale, in conjunction with imaging and geochemical data, the most plausible explanation for the origin of the Ransko Ni–Cu–PGE ores is a gravity-driven process where dense sulfide liquids percolate downward through the network of olivine-rich lithologies (e.g., Chung and Mungall 2009; Barnes et al. 2017, 2018; Mao et al. 2022; Zuccarelli et al. 2022) with evolutionary steps as follows.

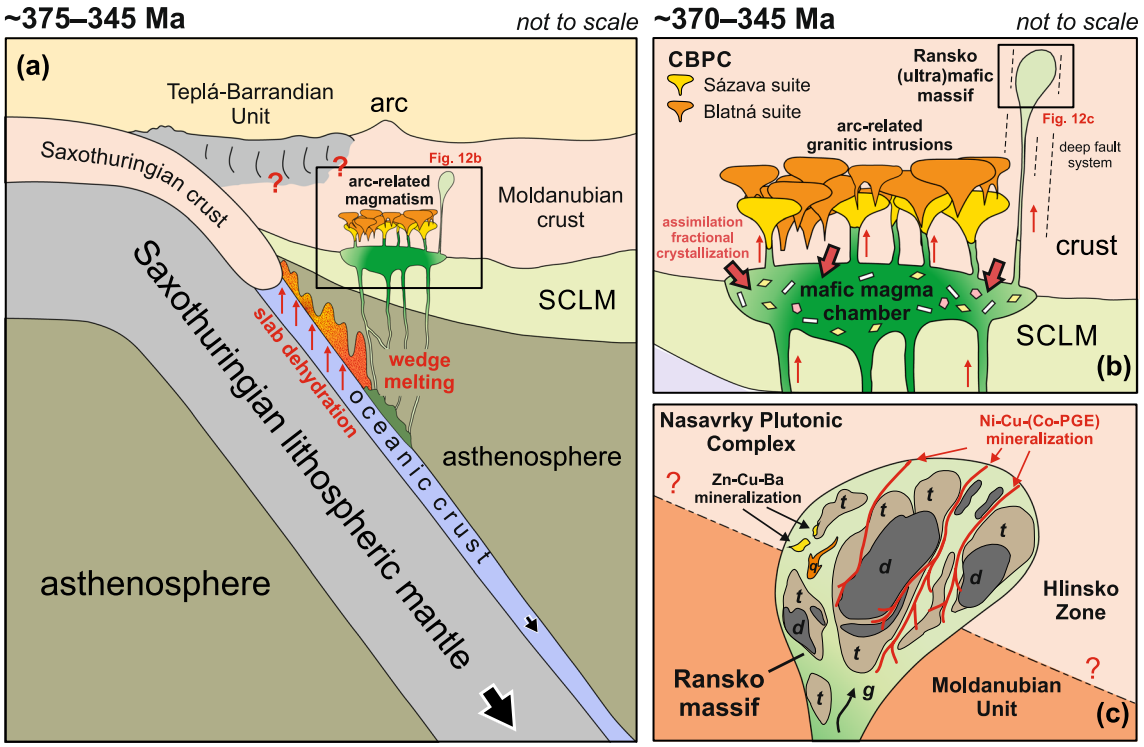

Fig. 12 Geodynamic model for the petrogenesis and evolution of the Ransko massif, its parental melts, and Ni–Cu–(Co–PGE)/Zn–Cu–Ba mineralizations with respect to Variscan evolution of the Bohemian Massif. The model invokes the formation of mafic melts in the sub-arc mantle during ~ 375 and 345 Ma (**a**) followed by their accumulation in the lower crust where they underwent moderate crustal assimilation connected with extensive fractional crystallization (**b**). Thereafter, the presence of a deep-crustal fault system permitted upward movement of evolved, water-rich over-pressurized, and sulfur-rich Ransko cumulate mafic melts followed by subsequent formation of Ni–Cu–PGE and Zn–Cu ores (**c**). See the text for more details. g – (olivine)gabbro, t – troctolite, d – dunite, q – quartz diorite, CBPC – Central Bohemian Plutonic Complex, SCLM – subcontinental lithospheric mantle

Between ~ 375 and 345 Ma, hydrous mafic melts were generated in the continental margin mantle wedge in response to the convergence of Saxothuringian Unit beneath the Moldanubian/Teplá–Barrandian units (Fig. 12a). These melts accumulated at the base of the lower crust where they caused underplating and associated melting to produce the most primitive members of the CBPC (Sázava suite), and underwent moderate crustal assimilation connected with extensive fractional crystallization (Fig. 12b). Very narrow range of $\delta^{34}S$ values (− 1.2‰ to + 0.4 ‰) reported for the Ransko Ni–Cu–PGE ores (Pašava et al. 2003) indicate either limited incorporation S-rich crustal lithologies or high silicate/sulfide mass ratio (R) during assimilation leading to re-equilibration of $\delta^{34}S$ to mantle-like values (e.g., Lesher and Burham 2001). The presence of a deep-crustal fault system likely permits recurrent upward movement (Pokorný 1969) of evolved, water- and sulfur-rich over-pressurized Ransko cumulate (ultra)mafic melts (e.g., Tornos et al. 2006) with lower crustal rock fragments (e.g., xenolith samples RAN-24 and RAN-27) to upper crustal conditions (Fig. 12b). Subsequent partial crystallization of the (ultra)mafic cumulates and precipitation of sulfide droplets forming disseminated Ni–Cu–PGE ores was followed by the accumulation of sulfide melt(s) at some places and their injection as downward percolated dense, low-viscosity sulfide liquids along NE–SW trending fracture networks. These also served as pathways for late-stage fluids that resulted in pervasive hydrothermal alteration expressed by extensive serpentinization, saussuritization, and uralitization as well as Zn–Cu–Ba fluids sometimes following the boundaries between (ultra) mafic lithologies and suggesting similar controlling mechanisms of mineralization (Fig. 12c). During this stage, disseminated or net-textured Ni–Cu–PGE ores (e.g., Barnes et al. 2017) were precipitated in the network of lithologically weakened (ultra)mafic cumulates depending on the amount of sulfide liquid present. Injection of hot sulfide liquids resulted in the replacement of the already altered plagioclase with the lowest melting temperature by a sulfide melt (Fig. 2d). Continuing downward percolation was responsible for the density-driven segregation and accumulation of sulfide liquids that formed massive ores (e.g., Zuccarelli et al. 2022). In plagioclase-rich cumulates (troctolites), the breakdown of plagioclase leads to local Al-oversaturation (e.g., Guo et al. 1996) expressed by the presence of euhedral inclusions of corundum observed within massive pyrrhotite-dominated ores (Fig. 5a).

Overall, the absence of vein-hosted sulfides and tectonised magmatic breccias at the Ransko massif argues against emplacement or remobilization of Ni–Cu–PGE during late magmatic and/or high temperature post-emplacement deformation stage (cf. Barnes et al. 2018).

At Jezírka deposit with the highest Ni + Cu value reported (up to 4 wt%), a particular vertical variation of Ni/Cu ratios is developed with the highest value (1.6) found at the surface and a downward decrease to 0.4 (Pokorný 1969). Such variability supports the model of Ni–Cu–PGE ore formation presented above as it can be best explained by the chemical changes during downward migration and assisted fractionation of sulfide liquid. In this respect, crystallization of Ni-rich monosulfide solid solution (MSS) in the shallower ore system resulted in the formation of relatively Cu-enriched residual sulfide liquid that continued to migrate downward producing low Ni/Cu ratios observed at the deeper parts of the deposit.

The enhanced fractionation of sulfide liquid that led to a redistribution of metals is further illustrated by PGE (Fig. 11) that are typically concentrated in immiscible sulfide liquids along with other metals (Naldrett 2010 and references therein). While the primitive-mantle normalized patterns of different rock and/or mineralization types exhibit similar characteristics with steep distributions from Os to Pd, massive and typically Ni-rich ores yield the highest I-PGE and Re contents that are largely correlated with S and partly also with Ni contents (Fig. 11a), indicative of scavenging and precipitation of these metals along with Ni-rich MSS. This agrees with in-situ laser ablation data collected for the Ransko sulfides (Pašava et al. 2023) that show the highest Os and Ir contents in pyrrhotite and pentlandite from massive ores whereas Ru appears to be dominantly bound to pentlandite. In contrast, the absence of correlations between Pt–Pd and sulfur, the presence of Pd–Bi–Te and Pt–As mineral paragenesis Fig. 5f, g) along with the occurrence of other tellurides of Bi, Pb, Ag, and Ni minerals, but the absence of elevated Pt and Pd contents in Cu-sulfides (Pašava et al. 2023) indicate scavenging and precipitation of Pt and Pd by late-stage, commonly Cu-rich, liquids at ~ 400–500 °C (Pašava et al. 2003). We note that the highest Pt and Cu contents at given (rather low) S contents (< 2 wt%) were found in dunites (up to ~ 120 ppb Pt and ~ 2,385 ppm Cu) which might indicate that these rock types serve as efficient traps for these metals.

Implications for the metallogeny of critical metals (Ni, Co, PGE) in Variscan basements

The orogenic type Ni–Cu–(Co–PGE) deposits have remained under-explored in comparison to world-class deposits that are related to extensive (ultra)mafic magmatic activity in rifted intracontinental settings with ~ 2.06 Ga Kevitsa in northern Finland (Luoavirta 2018) representing the sole currently exploited Ni–Cu–PGE deposit exploited in the EU member countries. This is due to a significantly low predicted economic potential of orogenic-type deposits, notably in terms of PGE.

Currently, three orogenic type Ni–Cu–(PGE) mineralizations have been identified within the European Variscan belt

(Fig. 1a): (1) Aguablanca in Spain (Tornos et al. 2006; Piña 2019), (2) Beja in Portugal (Jesus et al. 2016, 2020), and (3) Ransko in Czech Republic (this study; Mísař 1974; Pašava et al. 2003). Our observations indicate that these mineralizations share many similarities that might serve as markers for future exploration efforts. Notably, the complexes exhibit largely (ultra)mafic and predominantly cumulate compositions, have contemporaneous ages (Romeo et al. 2004; Jesus et al. 2007; Pin et al. 2008; Ackerman et al. 2013; this study), and were emplaced in a close relationship with widespread Andean-type continental magmatic arc granitic bodies. Furthermore, they share a similar composition of Ni–Cu–(PGE) ores and sulfide ore textures. On the other hand, it appears that only Aguablanca and Ransko deposits host significant Ni–Cu sulfide ore accumulations with the former showing the highest Pt and Pd contents (up to 3 g/t; Piña 2019) while the rather Ni–PGE-poor nature has been reported for sulfidic mineralization developed in at least the western part of the layered Beja complex (Jesus et al. 2020).

Thus, while the Variscan, arc-related (ultra)mafic magmatism has the potential to result in the formation of Ni–Cu–(PGE) ores, complex processes that interplay during the emplacement and evolution of the parental magmas hold the key to their significance. First, in contrast to the Beja complex where the Ni–Cu sulfides crystallized in-situ towards to the end of (ultra)mafic rocks fractional cycle at deep crustal conditions (Jesus et al. 2020), accumulations of Ni–Cu–(PGE) ores at Aguablanca and Ransko are related to the shallow evolution and gravitational percolation of sulfide liquids (Piña et al. 2006; Tornos et al. 2006; this study). The capability to not reach sulfide saturation at depth can be largely connected with water-rich conditions of the parental magmas considering that larger amounts of water are capable to dissolve a larger amount of sulfur that prevents magma from reaching sulfide saturation (Fortin et al. 2015). Together with the accumulation of large volumes of sulfide liquid(s) during the latest stages of the magmatic evolution, these phenomena can be one of the crucial aspects controlling the extent of sulfide mineralization. Second, all three massifs show several indices of crustal contamination (e.g., the presence of crustal xenoliths and orthopyroxene-bearing lithologies, only mildly radiogenic Hf–Nd values, and the chemistry of sulfides; Ackerman et al. 2013; Jesus et al. 2016; Pašava et al. 2023; Tornos et al. 2006; this study) suggesting a variable extent of interaction with surrounding lithologies at crustal levels. However, the extent and depth of assimilation as well as the nature of assimilants (for example, assimilation of reducing C-rich lithologies can promote sulfur solubility in the melt; Brenan and Caciagli 2000) preventing early sulfide saturation at the depth play a key role in a formation of PGE-rich magma (Jesus et al. 2020). Indeed, the formation of exceptionally Ni–Cu–(PGE)-rich ores developed at Aguablanca is connected with the excessive contamination of S-rich lithologies leading to the addition of 30% sulfur from the external source (Tornos et al. 2006) that might facilitate sulfur saturation at upper crustal conditions. In the case of the Ransko massif, its pipe-like shape (Fig. 12c) and the position on the deep-crustal NE–SW trending fault system (Mísař 1974) and emplacement at shallow levels may play a key role in the Ni–Cu–(PGE) ores metallogenesis.

Overall, our study highlights a large potential of orogenic type Ni–Cu–(PGE) deposits emplaced in Variscan, arc-related crustal domains across Europe. Considering also the mafic dykes and gabbro-related Ni–Cu–(PGE) occurrences reported from northern Bohemia and Saxony that are also related to arc-related magmatism (~ 390–350 Ma; Haluzová et al. 2015; Járóka et al. 2023), we suggest that Variscan metallogenetic potential needs to be reconsidered. Thus, new, specifically targeted studies related to less voluminous (ultra)mafic activity need to be conducted in this respect.

Conclusions

(1) Newly gathered Sm–Nd and U–Pb data on (ultra)mafic lithologies and cross-cutting granite porphyry and Re–Os age on molybdenite from the Ransko Zn–Cu–Ba mineralization, bracket the Variscan emplacement of the Ransko (ultra)mafic rocks and associated mineralization activity at ~ 370–345 Ma.

(2) Parental melts of the Ransko massif, composed of essentially cumulate (ultra)mafic rocks that underwent large-scale hydrothermal alteration, were generated at sub-arc mantle settings and underwent extensive modification through fractional crystallization and experienced a rather limited extent of crustal contamination.

(3) The spatial distribution of Ni–Cu–PGE ores together with their determined Variscan age, indicates their formation during the late stages of magmatic activity of the Ransko massif through the gravity-driven percolation along previously (hydrothermally) weakened structures associated with downward fractionation of sulfide liquids.

(4) The orogenic arc-related Ni–Cu–(PGE) mineralization at the Ransko massif shares many similarities with some other magmatic sulfide Ni–Cu deposits in the European Variscan Belt (e.g., Aguablanca, Beja) and our study highlights the potential of orogenic Ni–Cu occurrences for future exploration efforts keeping in mind that complex processes that interplay during the emplacement and evolution of the parental magmas hold the key to their significance.

Supplementary Information The online version contains supplementary material available at https://doi.org/10.1007/s00126-025-01353-z.

Acknowledgements The research was supported by Operational Programme Research, Innovation and Education, [CZ.02.1.01/0.0/0.0/

16_026/0008459 (Geobarr)] from the European Regional Development Fund, Strategic Research Plan of the Czech Geological Survey (DKRVO 2023–2027). LA acknowledges the institutional support through the RVO67985831. We are grateful to Veronika Renčiuková and Jan Rejšek (both from the Institute of Geology of the Czech Academy of Sciences, IG CAS) for the collection of Sr–Nd–Pb–Os isotopic data, Jana Ďurišová (IG CAS) and Ladislav Strnad (Charles University) for ICP-MS analyses, Ondřej Pour (Czech Geological Survey) for BSE images of photomicrographs of ore samples, Renata Čopjaková (Masaryk University) for EMP analyses, František Veselovský (Czech Geological Survey) for separation of ore and rock-forming minerals for geochronology and Jana Rajlichová (IG CAS) for the help with the figures.

Author contributions LA, VW, JN and PR designated and developed the research ideas and carried out the sampling. The first draft of the manuscript was written by LA, VW, MK and JN and was further developed by all authors. Mineral data analyses and interpretations was carried out by MK. U–Pb and Re–Os geochronology was performed by JM and RAC, respectively. Oxygen isotopic analyses was carried out by AP. VS performed geochemical trace element modelling. All authors read and approved the final manuscript.

Funding Open access publishing supported by the institutions participating in the CzechELib Transformative Agreement. This study has been funded by the European Union (SEMACRET, Grant Agreement no. 101057741) and UKRI.

Data availability All data collected within the framework of this study are listed in the manuscript.

Declarations

Conflicts of interests The authors declare no competing interests.

References

Ackerman L, Haluzová E, Creaser RA, Pašava J, Veselovský F, Breiter K, Erban V, Drábek M (2017) Temporal evolution of mineralization events in the Bohemian Massif inferred from the Re-Os geochronology of molybdenite. Miner Depos 52:651–662

Ackerman L, Kotková J, Čopjaková R, Sláma J, Trubač J, Dillingerová V (2020) Petrogenesis and Lu–Hf dating of (ultra)mafic rocks from the Kutná Hora Crystalline Complex: implications for the Devonian evolution of the Bohemian massif. J Petrol 61:egaa075.

Ackerman L, Pašava J, Erban V (2013) Re–Os geochemistry and geochronology of the Ransko gabbro–peridotite massif, Bohemian Massif. Miner Depos 48:799–804

Anczkiewicz R, Platt JP, Thirlwall MF, Wakabayashi J (2004) Franciscan subduction off to a slow start: evidence from high-precision Lu–Hf garnet ages on high grade-blocks. Earth Planet Sci Lett 225:147–161

Barnes SJ, Mungall JE, Le Vaillant M, Godel B, Lesher CM, Holwell D, Lightfoot PC, Krivolutskaya N, Wei B (2017) Sulfide-silicate textures in magmatic Ni-Cu-PGE sulfide ore deposits: Disseminated and net-textured ores. Am Mineral 102:473–506

Barnes SJ, Staude S, Le Vaillant M, Piña R, Lightfoot PC (2018) Sulfide-silicate textures in magmatic Ni-Cu-PGE sulfide ore deposits: Massive, semi-massive and sulfide-matrix breccia ores. Ore Geol Rev 101:629–651

Barnes SJ, Taranovic V, Miller JM, Boyce G, Beresford S (2020) Sulfide emplacement and migration in the Nova-Bollinger Ni-Cu-Co deposit, Albany-Fraser Orogen, Western Australia. Econ Geol 115:1749–1776

Beard JS (1986) Characteristic mineralogy of arc-related cumulate gabbros: implications for the tectonic setting of gabbroic plutons and for andesite genesis. Geology 14:848–851

Berndt J, Koepke J, Holtz F (2005) An experimental investigation of the influence of water and oxygen fugacity on differentiation of MORB at 200 MPa. J Petrol 46:135–167

Blichert-Toft J, Albarède F (1999) Hf isotopic compositions of the Hawaii Scientific Drilling Project Core and the source mineralogy of Hawaiian basalts. Geophys Res Lett 26:935–938

Boynton WV (1984) Cosmochemistry of the rare earth elements: meteorite studies. In: Henderson P (ed) Rare earth element geochemistry. Elsevier, Amsterdam, pp 63–114

Brenan JM, Caciagli NC (2000) Fe–Ni exchange between olivine and sulphide liquid: implications for oxygen barometry in sulphide-saturated magmas. Geochim Cosmochim Acta 64:307–320

Chauvel C, Blichert-Toft J (2001) A hafnium isotope and trace element perspective on melting of the depleted mantle. Earth Planet Sci Lett 190:137–151

Chung H-Y, Mungall JE (2009) Physical constraints on the migration of immiscible fluids through partially molten silicates, with special reference to magmatic sulfide ores. Earth Planet Sci Lett 286:14–22

Cohen AS, Waters FG (1996) Separation of osmium from geological materials by solvent extraction for analysis by thermal ionisation mass spectrometry. Anal Chim Acta 332:269–275

Cui M-M, Su B-X, Wang J, Chen K-Y, Sakyi PA, Tang D-M, Hu Y-P, Sun J-G, Cui J, Anani CY, Gao D-L (2020) Alaskan-type nature and PGE mineralization of the Wuxing mafic–ultramafic complex in eastern part of the Central Asian Orogenic belt. Ore Geol Rev 123:103566

Day JMD, Brandon AD, Walker RJ (2016) Highly siderophile elements in Earth, Mars, the Moon, and asteroids. Rev Mineral Geochemistry 81:161–238

Dempírová L, Šikl J, Kašičková R, Zoulková V, Kříbek B (2010) The evaluation of precision and relative error of the main components of silicate analyses in Central Laboratory of the Czech Geological Survey. Geosci Rep 27:326–330

Doe BR, Zartman RE (1979) Plumbotectonics: the Phanerozoic. In: Barnes HL (ed) Geochemistry of Hydrothermal Ore Deposits. Interscience, New York, pp 22–70

Fehlhaber K, Bird DK (1991) Oxygen-isotope exchange and mineral alteration in gabbros of the Lower Layered Series, Kap Edvard Holm Complex, East Greenland. Geology 19:819–822

Fortin MA, Riddle J, Desjardins-Langlais Y, Baker DR (2015) The effect of water on the sulfur concentration at sulfide saturation (SCSS) in natural melts. Geochim Cosmochim Acta 160:100–116

Gao JF, Wang HH (2024) Permian mafic-ultramafic magmatism and sulfide mineralization in the Central Asian Orogenic Belt: A review. J Asian Earth Sci 264:106071

Garuti G, Pushkarev EV, Zaccarini F, Cabella R, Anikina E (2003) Chromite composition and platinum-group mineral assemblage in the Uktus Uralian-Alaskan-type complex (Central Urals, Russia). Miner Depos 38:312–326

Guo J, O'Reilly SY, Griffin WL (1996) Corundum from basaltic terrains: A mineral inclusion approach to the enigma. Contrib to Mineral Petrol 122:368–386

Haluzová E, Ackerman L, Pašava J, Jonášová Š, Svojtka M, Hrstka T, Veselovský F (2015) Geochronology and characteristics of Ni-Cu-(PGE) mineralization at Rožany, Lusatian Granitoid Complex, Czech Republic. J Geosci 60:219–236

Himmelberg GR, Loney RA (1995) Characteristics and petrogenesis of Alaskan-type ultramafic-mafic intrusions, southeastern Alaska. USGS Prof Pap 1564.

Hollocher K, Robinson P, Walsh E, Roberts D (2012) Geochemistry of amphibolite-facies volcanics and gabbros of the støren nappe in extensions west and southwest of Trondheim, Western Gneiss Region, Norway: A key to correlations and paleotectonic settings. Am J Sci 312:357–416

Holub M, Jelínek E, Komínek E, Pluskal O (1992) Genetic model of sulfide mineralization of the Ransko gabbro peridotite massif (Bohemia, Czechoslovakia). Sbor Geol Věd LG 30:7–42

Holub M, Pokorný J (1970) Alternation of gabbros and troctolites and genesis of sulfides in the Ransko basic massif. Sbor Geol Věd LG 11:99–111

Hudson DR (1972) Evaluation of genetic models for Australian sulphide nickel deposits. In: Australasian Institute of Mining and Metallurgy (AuSIMM) Abstracts. Newcastle, pp 59–68

Irvine TN, Baragar VNA (1971) A guide to the chemical classification of the common volcanic rocks. Can J Earth Sci 8:523–548

Jackson SE, Pearson NJ, Griffin WL, Belousova EA (2004) The application of laser ablation-inductively coupled plasma-mass spectrometry to in situ U-Pb zircon geochronology. Chem Geol 211:47–69

Janoušek V, Bowes DR, Rogers G, Farrow CM, Jelínek E (2000) Modelling diverse processes in the petrogenesis of a composite batholith: the Central Bohemian Pluton, Central European Hercynides. J Petrol 41:511–543

Janoušek V, Braithwaite CJR, Bowes DR, Gerdes A (2004) Magma-mixing in the genesis of Hercynian calc-alkaline granitoids: an integrated petrographic and geochemical study of the Sázava intrusion, Central Bohemian Pluton, Czech Republic. Lithos 78:67–99

Janoušek V, Erban Kochergina YV, Andronikov AV, Kusbach VK (2022) Decoupling of Mg from Sr–Nd isotopic compositions in Variscan subduction-related plutonic rocks from the Bohemian Massif: implications for mantle enrichment processes and genesis of orogenic ultrapotassic magmatic rocks. Int J Earth Sci 111:1491–1518

Janoušek V, Wiegand BA, Žák J (2010) Dating the onset of Variscan crustal exhumation in the core of the Bohemian Massif: new U-Pb single zircon ages from the high-K calc-alkaline granodiorites of the Blatná suite, Central Bohemian Plutonic Complex. J Geol Soc London 167:347–360

Járóka T, Pfänder JA, Seifert T, Hauff F, Sperner B, Staude S, Stephan T, Schulz B (2023) Age and petrogenesis of Ni-Cu-(PGE) sulfide-bearing gabbroic intrusions in the Lausitz Block, northern Bohemian Massif (Germany/Czech Republic). Lithos 444–445:107090

Jesus AP, Mateus A, Benoit M, Tassinari C, Santos T (2020) The timing of sulfide segregation in a Variscan synorogenic gabbroic layered intrusion (Beja, Portugal): Implications for Ni-Cu-PGE exploration in orogenic settings. Ore Geol Rev 126:103767

Jesus AP, Mateus A, Munhá JM, Tassinari C, Santos T (2016) Evidence for underplating in the genesis of the Variscan synorogenic Beja Layered Gabbroic Sequence (Portugal) and related mesocratic rocks. Tectonophysics 683:148–171

Jesus AP, Munhá J, Mateus A, Tassinari C, Nutman AP (2007) The Beja Layered Gabbroic Sequence (Ossa-Morena Zone, Southern Portugal): geochronology and geodynamic implications. Geodin Acta 20:139–157

Johan Z (2002) Alaskan-type complexes and their platinum-group element mineralization. In: Cabri L (ed) The geology, geochemistry, mineralogy and mineral beneficiation of platinum-Group elements. Canadian Institute of Mining, Metallurgy and Petroleum, pp 669–719

Keays RR, Lightfoot PC (2010) Crustal sulfur is required to form magmatic Ni-Cu sulfide deposits: Evidence from chalcophile element signatures of Siberian and Deccan Trap basalts. Miner Depos 45:241–257

Kubeš M, Leichmann J, Kotková J, Čopjaková R, Holá M, Sláma J (2022) Diversity of origin and geodynamic evolution of the mantle beneath the Variscan Orogen indicating rapid exhumation within subduction-related mélange (Moldanubian Zone, Bohemian Massif). Lithos 422–423:106726

Leake BE, Woolley AR, Arps CES, Birch WD, Gilbert MC, Grice JD, Hawthorne FC, Kato A, Kisch HJ, Krivovichev VG, Whittaker EJW, Youzhi G (1997) Nomenclature of amphiboles: Report of the subcommittee on amphiboles of the international mineralogical association, commission on new minerals and mineral names. Can Mineral 35:219–246

Lesher CM, Burnham OM (2001) Multicomponent elemental and isotopic mixing in Ni-Cu-(PGE) ores at Kambalda, Western Australia. Can Mineral 39:421–446

Li C, Ripley EM (2011a) The giant Jinchuan Ni-Cu-(PGE) deposit: tectonic setting, magma evolution, ore genesis, and exploration implications. Magmat. Ni-Cu PGE Depos. Geol Geochemistry, Genes 17:163–180

Li C, Ripley EM (2011b) Magmatic Ni-Cu and PGE deposits: geology, geochemistry, and genesis. Society of Economic Geologists

Lu Y, Lesher CM, Deng J (2019) Geochemistry and genesis of magmatic Ni-Cu-(PGE) and PGE-(Cu)-(Ni) deposits in China. Ore Geol Rev 107:863–887

Ludwig KR (2008) Isoplot 4.00: A geochronological toolkit for Microsoft Excel. Berkeley

Luoavirta K (2018) Magmatic evolution of the Kevitsa igneous complex, northern Finland, and itsrelation to the associated Ni-Cu-(PGE) mineralization. Dissertation. University of Oolu

Maier WD, Barnes SJ, Chinyepi G, Barton JM, Eglington B, Satshedi I (2008) The composition of magmatic Ni-Cu-(PGE) sulfide deposits in the Tati and Selebi-Phikwe belts of eastern Botswana. Miner Depos 43:37–60

Mao Y-J, Barnes SJ, Godel B, Schoneveld L, Qin K-Z, Tang D, Williams D, Kang Z (2022) Sulfide ore formation of the Kalatongke Ni-Cu deposit as illustrated by sulfide textures. Econ Geol 117:1761–1778

Marek F (1970) Estimate of the age of the Ransko basic massif based on paleomagnetic data. Věstník Ústředního Ústavu Geol 45:99–102

Markey R, Stein HJ, Hannah JL, Zimmerman A, Selby D, Creaser RA (2007) Standardizing Re–Os geochronology: a new molybdenite reference material (Henderson, USA) and the stoichiometry of Os salts. Chem Geol 244:74–87

Matte P (2001) The Variscan collage and orogeny (480–290 Ma) and the tectonic definition of the Armorica microplate: A review. Terra Nov 13:122–128.

Mattey D, Lowry D, Macpherson C (1994) Oxygen isotope composition of mantle peridotite. Earth Planet Sci Lett 128:231–241

Middlemost EAK (1994) Naming materials in the magma/igneous rock system. Earth Sci Rev 37:215–224. https://doi.org/10.1016/0012-8252(94)90029-9

Mísař Z (1974) The Ransko gabbro–peridotite massif and its mineralization (Czechoslovakia). Charles University
Morimoto N (1988) Nomenclature of pyroxenes. Mineral Mag 52:535–550
Mundl A, Ntaflos T, Ackerman L, Bizimis M, Bjerg EA, Wegner W, Hauzenberger CA (2016) Geochemical and Os-Hf-Nd-Sr isotopic characterization of North Patagonian mantle xenoliths: Implications for extensive melt extraction and percolation processes. J Petrol 57:685–715
Nahodilová R, Hasalová P, Štípská P, Schulmann K, Závada P, Míková J, Kylander-Clark A, Maierová P (2020) Exhumation of subducted continental crust along the arc region. Gondwana Res 80:157–187
Nakanishi N, Yokoyama T, Ishikawa A (2019) Refinement of the micro-distillation technique for isotopic analysis of geological samples with pg-level osmium contents. Geostand Geoanalytical Res 43:231–243
Naldrett AJ (1973) Nickel sulphide deposits: Classification, composition, and genesis. Can Inst Mining, Metall Pet CIM Bull 66:45–63
Naldrett AJ (2010) Magmatic sulfide deposits. Springer-Verlag, Berlin Heidelberg
Pack A, Tanaka R, Hering M, Sengupta S, Peters S, Nakamura E (2016) The oxygen isotope composition of San Carlos olivine on the VSMOW2-SLAP2 scale. Rapid Commun Mass Spectrom 30:1495–1504
Pašava J, Andronikova I, Wertich V, Ackerman L, Rambousek P, Pour O, Malý K (2023) Chemistry of major sulfides from Ni-Cu (PGE) mineralization at the Ransko ore district (Bohemian Massif): A result from LA ICPMS study. In: Proceedings of the 17th SGA Biennial Meeting. pp 191–195
Pašava J, Vavřín I, Frýda J, Janoušek V, Jelínek E (2003) Geochemistry and mineralogy of Platinum-group elements in the Ransko gabbro–peridotite massif, Bohemian Massif (Czech Republic). Miner Depos 38:298–311
Paton C, Hellstrom J, Paul B, Woodhead J, Hergt J (2011) Iolite: Freeware for the visualisation and processing of mass spectrometric data. J Anal at Spectrom 26:2508–2518
Pearce JA (2008) Geochemical fingerprinting of oceanic basalts with applications to ophiolite classification and the search for Archean oceanic crust. Lithos 100:14–48
Peltonen P (1995) Petrogenesis of ultramafic rocks in the Vammala Nickel Belt: Implications for crustal evolution of the early Proterozoic Svecofennian arc terrane. Lithos 34:253–274
Pin C, Fonseca PE, Paquette JL, Castro P, Matte P (2008) The ca. 350 Ma Beja Igneous Complex: A record of transcurrent slab break-off in the Southern Iberia Variscan Belt? Tectonophysics 461:356–377
Pin C, Gannoun A, Dupont A (2014) Rapid, simultaneous separation of Sr, Pb, and Nd by extraction chromatography prior to isotope ratios determination by TIMS and MC-ICP-MS. J Anal at Spectrom 29:1858–1870
Piña R (2019) The Ni-Cu-(PGE) Aguablanca Ore Deposit (SW Spain). Springer
Piña R, Lunar R, Ortega L, Gervilla F, Alapieti T, Martínez C (2006) Petrology and geochemistry of mafic-ultramafic fragments from the Aguablanca Ni-Cu ore breccia, southwest Spain. Econ Geol 101:865–881
Pitra P, Guiraud M (1996) Probable anticlockwise P-T evolution in extending crust: Hlinsko region. J Metamorph Geol 14:49–60
Pokorný J (1969) Sulphide ore deposits in the Ransko basic massif. Sborník Geol Věd Ústředního Ústavu Geol Řada Ložiskové Geol 10:111–154
Ribeiro A, Munhá J, Dias R, Mateus A, Pereira E, Ribeiro L, Fonseca P, Araújo A, Oliveira T, Romão J, Coke C, Pedro J (2007) Geodynamic evolution of the SW Europe Variscides. Tectonics 26:TC6009.
Romeo I, Lunar R, Capote R, Quesada C, Dunning GR, Piña R, Ortega L (2004) Edades de cristalización U-Pb en circones del complejo ígneo de Santa Olalla de Cala: Implicaciones en la edad del yacimiento de Ni-Cu-EGP de Aguablanca (Badajoz). In: Macla. pp 29–30
Salters VJM (1996) The generation of mid-ocean ridge basalts from the Hf and Nd isotope perspective. Earth Planet Sci Lett 141:109–123. https://doi.org/10.1016/0012-821X(96)00070-2
Schulmann K, Edel JB, Martínez Catalán JR, Mazur S, Guy A, Lardeaux JM, Ayarza P, Palomeras I (2022) Tectonic evolution and global crustal architecture of the European Variscan belt constrained by geophysical data. Earth-Science Rev 234:104195
Selby D, Creaser RA (2004) Macroscale NTIMS and microscale LA-MC-ICP-MS Re-Os isotopic analysis of molybdenite: Testing spatial restrictions for reliable Re-Os age determinations, and implications for the decoupling of Re and Os within molybdenite. Geochim Cosmochim Acta 68:3897–3908
Sláma J, Košler J, Condon DJ, Crowley JL, Gerdes A, Hanchar JM, Horstwood M, Morris GA, Nasdala L, Norberg N, Schaltegger U, Schoene B, Tubrett MN, Whitehouse M (2008) Plešovice zircon — A new natural reference material for U-Pb and Hf isotopic microanalysis. Chem Geol 249:1–35
Sláma J, Walderhaug O, Fonneland H, Kosler J, Pedersen RB (2011) Provenance of Neoproterozoic to upper Cretaceous sedimentary rocks, eastern Greenland: Implications for recognizing the sources of sediments in the Norwegian Sea. Sediment Geol 238:254–267
Soejono I, Collett S, Kohút M, Janoušek V, Schulmann K, Bukovská Z, Novotná M, Zelinková T, Míková J, Hora JM, Veselovský F (2024) Paleogeography of the Gondwana passive margin fragments involved in the Variscan and Alpine collisions: Perspectives from metavolcanic-sedimentary basement of the Western Carpathians. Earth-Science Rev 253:104763
Stacey JS, Kramers JD (1975) Approximation of terrestrial lead geochemistry of the Sung Valley carbonatite complex, Shilong, isotope evolution by a two-stage model. Earth Planet Sci Lett 26:207–221
Štědrá V, Břízová E, Fürych V, Hanžl P, Kadlecová R, Kirchner K, Lysenko V, Mrnková J, Rambousek P, Roštínský P, Skácelová D, Skácelová Z, Valigurský L, Verner K, Zelenka P (2009) Geological map of the Czech Republic 1:25 000, 23–221 Ždírec nad Doubravou.
Strnad L, Mihaljevič M, Šebek O (2005) Laser ablation and solution ICP-MS determination of rare earth elements in USGS BIR-1G, BHVO-2G and BCR-2G glass reference materials. Geostand Geoanalytical Res 29:303–314
Sun S, McDonough WF (1989) Chemical and isotopic systematics of oceanic basalts: implications for mantle composition and processes. In: Saunders AD, Norry M (eds) Magmatism in the Ocean Basins. Geological Society of London Special Publication, pp 313–345
Synek J, Oliveriová D (1993) Terrane character of the north-east margin of the Moldanubian Zone: the Kutná Hora Crystalline Complex, Bohemian Massif. Geol Rundschau 82:566–582. https://doi.org/10.1007/BF00212417
Thakurta J, Ripley EM, Li C (2008) Geochemical constraints on the origin of sulfide mineralization in the Duke Island Complex, southeastern Alaska. Geochemistry, Geophys Geosystems 9:Q07003
Tornos F, Galindo C, Casquet C, Rodríguez Pevida L, Martínez C, Martínez E, Velasco F, Iriondo A (2006) The Aguablanca Ni-(Cu) sulfide deposit, SW Spain: Geologic and geochemical

controls and the relationship with a midcrustal layered mafic complex. Miner Depos 41:737–769

Ulmer P, Kaegi R, Müntener O (2018) Experimentally derived intermediate to silica-rich arc magmas by fractional and equilibrium crystallization at 1.0 GPa: an evaluation of phase relationships, compositions, liquid lines of descent and oxygen fugacity. J Petrol 59:11–58

Vavřín I, Frýda J (1998) Pd-Pt-As-Te mineralizace na ložiskách měďnato-niklových rud z Kunratic a Rožan na Šluknovsku. Bull Czech Geol Sur 73:177–180

Venera Z, Schulmann K, Kröner A (2000) Intrusion within a transtensional tectonic domain: The Čistá granodiorite (Bohemian Massif)-structure and rheological modelling. J Struct Geol 22:1437–1454

Vervoort JD, Patchett PJ, Blichert-Toft J, Albarede F (1999) Relationships between Lu–Hf and Sm–Nd isotopic systems in the global sedimentary system. Earth Planet Sci Lett 168:79–99

Vondrovic L, Verner K, Buriánek D, Halodová P, Kachlík V, Míková J (2011) Emplacement, structural and P-T evolution of the ~346 Ma Miřetín Pluton (eastern Teplá-Barrandian Zone, Bohemian Massif): Implications for regional transpressional tectonics. J Geosci 56:343–357

Wiedenbeck M, Allé P, Corfu F, Griffin WL, Meier M, Oberli F, von Quadt A, Roddick JC, Spiegel W (1995) Three natural zircon standards for U-Th–Pb, Lu–Hf, trace element and REE analyses. Geostand Newsletter-the J Geostand Geoanalysis 19:1–23

Žák J, Kratinová Z, Trubač J, Janoušek V, Sláma J, Mrlina J (2011) Structure, emplacement, and tectonic setting of Late Devonian granitoid plutons in the Tepla-Barrandian unit, Bohemian Massif. Int J Earth Sci 100:1477–1495

Žák J, Verner K, Janoušek V, Holub FV, Kachlík V, Finger F, Hajná J, Tomek F, Vondrovic L, Trubač J (2014) A plate-kinematic model for the assembly of the Bohemian Massif constrained by structural relationships around granitoid plutons. Geol Soc London, Spec Publ 405:169–196

Zhao Y, Liu S-A, Xue C, Brzozowski MJ, Chen J (2024) Metasomatized mantle facilitates the genesis of magmatic nickel–copper sulfide deposits in orogenic belts: A copper isotope perspective. Geochim Cosmochim Acta 366:128–140

Zindler A, Hart S (1986) Chemical geodynamics. Annu Rev Earth Planet Sci 14:493–571

Zuccarelli N, Lesher CM, Houlé MG, Weston M, Barnes SJ (2022) Diversity of net-textured sulfides in magmatic sulfide deposits: insights from the Eagle's Nest Ni-Cu-(PGE) deposit, McFaulds Lake Greenstone Belt, Superior Province, Canada. Econ Geol 117:1731–1759